This is a non-typeset finally accepted version of this paper:

Rummel, L., Kaus, B.J.P., Baumann, T.S., White, R.W., Riel, N., 2020. Insights into the compositional evolution of crustal magmatic systems from coupled petrological-geodynamical models. Journal of Petrology, Volume 61, Issue 2, February 2020, egaa029. https://doi.org/10.1093/petrology/egaa029

Insights into the compositional evolution of crustal magmatic systems from coupled petrological-geodynamical models

Lisa Rummel[1,2]*, Boris J. P. Kaus[1,2], Tobias S. Baumann[1], Richard W. White[1,2,3], Nicolas Riel[1]

[1] Institute of Geosciences, Johannes Gutenberg University of Mainz, 55128 Mainz, Germany

[2] VAMOS Research Center, 55128 Mainz, Germany

[3] School of Earth & Environmental Sciences, University of St Andrews, KY16 9AL, Scotland, UK

*Corresponding author: lisarummel@gmx.de

Short title: Evolution of crustal magmatic systems

The evolution of crustal magmatic systems is incompletely understood, as most studies are limited either by their temporal or spatial resolution. Exposed plutonic rocks represent the final stage of a long-term evolution punctuated by several magmatic events with different chemistry and generated under different mechanical conditions. Although the final state can be easily described, the nature of each magmatic pulse is more difficult to retrieve. This study presents a new method to investigate the compositional evolution of plutonic systems while considering thermal and mechanical processes. A thermomechanical code (MVEP2) extended by a semi-analytical dike/sill formation algorithm, is combined with a thermodynamic modelling approach (Perple_X) to investigate the feedback between petrology and mechanics. Melt is extracted to form dikes while depleting the source region. The evolving rock compositions are tracked on markers using a different phase diagram for each discrete bulk-rock composition. The rock compositional evolution is thus tracked with a high precision by means of a database with more than 58,000 phase diagrams. This database describes how density, melt fraction, chemical composition of melt and solid fractions and mineralogical assemblages change over crustal to uppermost mantle *P-T* conditions for a large range of rock compositions. Each bulk rock composition is composed of the 10 major oxides (SiO_2-TiO_2-Al_2O_3-Cr_2O_3-MgO-FeO-CaO-Na_2O-K_2O-H_2O) including an oxygen buffer. The combined modelling approach is applied to study the chemical evolution of the crust during arc magmatism and related melt extraction and magma mixing processes. Basaltic sills are periodically injected into the crust to model heat/magma influx from the mantle. We find that accumulated sills turn into long-lived mush chambers when using a lower rock cohesion or assuming a higher intrusion depth. Associated partial melting of crustal host rocks occurs around densely distributed dikes and sills. High silica rocks (e.g. granites) are generated by partial melting of the host rocks, melt segregation within dikes, and from fractional crystallization of basalts. Although the volume of these rocks is relatively small in our models compared to rocks with a mafic to intermediate

composition, they provide important information about the processes of magma differentiation within arc continental crust.

Key words: coupled petrological-geodynamical models; depletion of rocks through diking; highly evolved rocks; large phase diagram database; long-lived mush chambers

INTRODUCTION

The prevailing views about the existence of long-lived, liquid-dominated magma chambers, have evolved drastically in the last decades. It is widely accepted that dike-and-sill networks exist throughout broad regions of the crust, with magma storage levels from the uppermost mantle to the upper crust (e.g. Cashman et al., 2017; Putirka, 2017). Different numerical and geochemical studies of exposed lower arc crust indicate that magma reservoirs are assembled by magma pulses, and thus formed incrementally (e.g. Leuthold et al., 2012; Blundy and Annen, 2016; Coleman et al., 2016). It is assumed that for most of its time a magma reservoir is in a mush-like state consisting of a pervasive crystalline framework (Bachmann and Bergantz, 2004; Bergantz et al., 2015) with only few percent of melt (e.g. Huang et al., 2015) forming only ephemerally eruptible, liquid-dominated bodies (e.g. Putirka, 2017; Cooper, 2017; Sparks and Cashman, 2017). Magma chambers may be formed by one of the two following mechanisms: incremental intrusion of magma into sub-solidus rocks, or melt segregation and rapid merging of melt-rich layers within mush regions (e.g. Sparks and Cashman, 2017). Within the mush, several processes may take place, such as, partial melting, fractional crystallization, magma mixing, melt segregation and solid compaction, magma influx, and entrainment of older plutonic crust and/or host rocks (e.g. Hildreth and Moorbath, 1988; Annen et al., 2015). State of the art studies focusing on silicic magma reservoirs are summarized in Bachmann and Huber (2016). The arc magmatism itself is highly episodic at all scales (temporal and spatial): in the production of melt, the growth of the magmatic system and the associated volcanic eruptions (e.g. Paterson and Ducea, 2015; De Silva et al., 2015). As most of the magmatic products in arcs crystallize before ever reaching the Earth's surface (only 3-4% erupts, e.g. Paterson and Ducea, 2015), it is important to model the development and

evolution of plutonic systems, in order to understand their link with surface eruptions and their structural significance upon the Earth's crustal differentiation.

Magmatic or plutonic systems can be investigated by looking at exposed plutonic bodies and volcanic rocks to study ancient magmatic systems (e.g. Paterson et al., 2011; Leuthold et al., 2012; Jagoutz, 2014; Cooper, 2017), or by directly addressing active systems through geodetic, seismic, gravity and magnetotelluric measurements (e.g. Lees, 2007; Hill et al., 2009; Pritchard and Gregg, 2016; Kiser et al., 2016; Biggs and Pritchard, 2017). Furthermore, the general dynamics of magmatic systems can be investigated with numerical simulations. Previous studies focus on thermal processes (e.g. Paterson et al., 2011; Annen et al., 2015; Karakas et al., 2017), mechanics of dike initiation and propagation (e.g., Gudmundsson, 2006; Rivalta et al., 2015; Gerbault et al., 2018), or processes inside the magma reservoir such as crystal/bubble evolution, chemical interaction and compaction processes (e.g. Solano et al., 2012, 2014; Huber and Parmigiani, 2018; Jackson et al., 2018; Riel et al., 2018; Schmeling et al., 2019). Most geodynamic models focus on the thermomechanical aspects, and do not consider the compositional variability of the system, and where phase diagrams are employed, their number is relatively small. Phase diagrams in these models are often incorporated as lookup tables, which were precomputed over a prescribed *P-T* range and for limited bulk rock compositions (e.g. Kaus et al. 2004; Rüpke et al., 2004; Yamato et al., 2007; Magni et al., 2014; Rummel et al., 2018; Piccolo et al., 2019). These lookup tables can be used to track the chemical evolution of extracted melts, as it was shown by Rummel et al. (2018) for a rising mantle plume. However, the usage of such phase diagrams is still not standard and simplified melt parameterizations (e.g. from Katz et al., 2003) are often employed without considering the evolving chemistry of the melt and residuum. To investigate the evolution of a crustal magmatic system and to understand the interactions between mechanical, thermal and chemical processes, the coupling between petrological (thermodynamic) and geodynamic

models is required. Quantifying conditions for magma storage, magma pathways and other processes that affect the efficiency of magma transport to the surface such as stress conditions, is critical to better understand the compositional evolution of magma and cumulates in the magma reservoir. Although new advances have been made in coupling thermodynamics with geodynamics (e.g. Tirone et al., 2009; Hebert et al., 2009; Duesterhoeft et al., 2014; Oliveira et al., 2017; Riel et al., 2018), it is still a challenge to do this for a chemical (and realistic) system with a large number of oxides as it results in a massive increase of computation time. To accurately track both the chemical/mineralogical and the mechanical evolution, we developed a new parallel framework to establish a phase diagram database covering the chemical range of magmatic systems. We use a suitable Gibbs free energy minimization program to compute those phase diagrams for a broad range of rock compositions, Perple_X (Connolly, 2005, 2009). Recent advances in extending melting models from metapelitic rocks (White et al., 2001, 2014) to mantle rocks (Jennings and Holland, 2015), metabasic rocks (Green et al., 2016), or even for this whole range (Holland et al., 2018), opens new perspectives for thermodynamic modelling over large *P*-*T* and compositional fields.

In this study, we investigate both the mechanical and chemical/mineralogical evolution of a magmatic system by focusing on a dike-sill network formed through mantle-derived magma influx into the crust. The paper describes the model approach and how phase diagrams can be coupled with thermo-mechanical models of magmatic systems. The potential application of this combined approach is illustrated with different examples. For instance, we explored the role of different parameters such as initial composition, intrusion rate, -temperature and -depth as well as rock cohesion and background strain rate which control the mechanics of the system. In the discussion, the sensitivity of the different model parameters on the evolving rock compositions is assessed and their relevance for continental crustal evolution is presented.

THERMODYNAMIC AND GEODYNAMIC MODELLING APPROACHES

The evolution of crustal magmatic systems is strongly affected by the mechanics of the lithosphere as well as by chemical differentiation. To model the evolution of those systems, we integrate thermodynamic rock properties (computed with Perple_X, Connolly, 2005, 2009) into a 2D geodynamic code (MVEP2, Kaus, 2010; Thielmann and Kaus, 2012). The geodynamic code solves the conservation equations of mass, momentum and energy for a visco-elasto-plastic rheology and is combined with a semi-analytical fracture opening algorithm (Sun, 1969) to simulate dike/sill formation (Rozhko et al., 2007). We focus here on the mechanical and chemical evolution of plutonic systems after mantle-derived basaltic magma has been intruded into horizontally opened fractures (sills) at depths ranging from the uppermost mantle to the upper crust. The ascent of basaltic magma through the mantle from its melting source depth in the mantle is not taken into account. The stress field around the intruded sills determines if and where mode-1 fractures will be formed to transport magma toward shallower crustal levels. Depending on the crack propagation direction, as influenced by the local stress field, vertically or horizontally oriented magma-filled fractures are formed. Here, magma-filled fractures that are generated from the sills or from partially molten host rocks are called “dikes”, irrespective of their orientation. These dikes are subdivided into first- and second-generation structures. The second generation describes dikes that are formed from those of the first generation. When melt is extracted to form dikes, the source region becomes depleted (the term source region is used here to describe an area from which melt can be extracted). This process produces a large diversity of new rock compositions, which are tracked on markers (marker-in-cell method) using a different phase diagram for each discrete chemical composition in the geodynamic model. For this, a database with more than 58,000 phase

diagrams has been created. Each of those phase diagrams is computed for one specific bulk rock composition and describes the evolution of density, melt fraction as well as chemistry and mineralogy over crustal to uppermost mantle *P*-*T* conditions.

Thermodynamic modelling

Thermodynamic modelling is achieved using the Gibbs free energy minimization program Perple_X 6.7.9 (Connolly, 2005, 2009). We use the Holland & Powell (2011) internally consistent thermodynamic data for endmembers (thermodynamic data file used: "hp622ver") and the activity-composition models for solid-solution phases are given in Table B1 (see Supplementary Data B). The chemical system used is: SiO_2-TiO_2-Al_2O_3-Cr_2O_3-FeO-MgO-CaO-Na_2O-K_2O-H_2O but is reduced depending on the composition for which the respective employed melting models are calibrated. For instance, available mantle melting excludes K_2O, TiO_2 and H_2O (Jennings and Holland, 2015) and melting of more evolved mafic magmatic rocks (Green et al., 2016) does not consider Cr_2O_3. The mantle model (Jennings and Holland, 2015) is only used in our models to compute the initial phase diagram of the mantle, whereas for all other rock compositions the model for metabasic rocks (Green et al., 2016) is used. The system is buffered along the QFM (quartz-fayalite-magnetite) oxygen buffer for simplicity, rather than explicitly considering Fe_2O_3 as an extensive system component. The incorporation of oxygen is required, because it strongly affects phase relations (e.g. Ulmer et al., 2018), and thus the solidus temperature. The total amount of melt and its density and chemistry are taken from both melting models (melt(G) or Melt(JH), Table B1, see Supplementary Data B) and from potentially stable endmember phases (e.g., albite liquid). The solid density and composition are computed from the whole system by subtracting the melt proportion. We compute thermodynamic properties on a grid with a final resolution of 257×257 points. With

a pressure range of 0.1-3000 MPa and a temperature range of 290-1900 K, thermodynamic properties are determined every 11.7 MPa and 6.3 K. At this resolution, the computation time is reasonable (~10 h on average) and all phase boundaries are resolved with a sufficient precision.

For the geodynamic simulations, we assume the continental crust to consist of an upper, middle and lower crust, using average compositions after Rudnick and Gao (2003). The magma in injected sills has a basaltic composition (Le Maitre, 1976). We add between 0.1 and 5 wt% H_2O to the crustal material and 1 or 5 wt% H_2O to the basalt. The chosen higher H_2O content in the basalt is based on arc related studies (e.g. Pichavant et al., 2002; Plank et al., 2013). The H_2O concentration describes the amount of H_2O available in the system, but the water capacity can be lower at specific *P*-*T* conditions. At sub-solidus conditions free water might exist (see Fig. B1, Supplementary Data B) and thus not all of the H_2O is stored in minerals and excess water is therefore removed from the system. The mantle has a pyrolitic composition after McDonough and Sun (1995). The rock compositions outlined above (Table 1) are used to compute the initial phase diagrams employed in the geodynamic simulations.

As soon as melt is extracted from a partially molten/crystallized region in the geodynamic simulation, the bulk rock chemistry of the initial stage changes and new phase diagrams are required to track the subsequent rock evolution. The extracted melt fills an opened tensile (mode-1) fracture and we assume that all melts were homogeneously mixed in the source prior to extraction. Depending on the *P*-*T* condition at which melt is extracted, the amount of extracted melt and the melt chemistry is different. The remaining solid (residuum) composition is directly related to the extracted melt, and may thus vary strongly between markers depending on the amount and composition of extracted melt. Therefore, a single generated dike (thermodynamically described with one phase diagram) leaves behind a depleted source with strongly variable composition. For all these chemically different stages,

a different phase diagram is needed that describes how solid and liquid compositions as well as density, melt fraction and stable mineral assemblage will evolve over a prescribed *P-T* range. The chemical evolution of the liquid and cumulate fraction as well as the change in phase properties with increasing temperature or silicon concentration are illustrated in Figure 1 and in Figure 2 for the basaltic rock composition (or for the middle crust, see Fig. A1 in Supplementary Data A). Figure 2 shows additionally the melt fraction evolution of the liquid and cumulate fraction for different depletion stages of the basalt. All computed phase diagrams are stored in a database (more than 58,000 in total) that is used in the geodynamic simulations. To establish such a large database, the computation of phase diagrams is executed in parallel. The bulk rock compositions used in the phase diagrams, are either compositions requested from previously executed geodynamic simulations or were randomly determined within the relevant compositional parameter space. The procedure of how to establish and to extend the database efficiently is beyond the scope of this paper and is not further detailed. Here, it is only important that the phase diagrams available in the database cover all relevant rock compositions to track all the possible sources, residue, cumulate and melt compositions of the magmatic system.

Geodynamic modelling

General method

The geodynamic modelling utilises the finite element code MVEP2[1] (Kaus, 2010; Thielmann and Kaus, 2012), in which tracers (marker-in-cell-technique) are used to track evolving rock properties (melt fraction, density, chemistry and mineralogy). The geodynamic model employs a computational mesh of around 400×350 finite elements with a resolution of ~125 m

[1] code is available at: https://bitbucket.org/bkaus/mvep2

horizontal and ~115 m vertical. The compositions are tracked on markers of which there are initially 1.3 million distributed over the model domain, but the number of markers increases during the simulations as new dikes/sills are generated. A semi-analytical algorithm for fracture opening and thus dike/sill formation is incorporated into the 2D visco-elasto-plastic thermo-mechanical models. The 2D code solves the governing conservation equations of mass, momentum and energy of slowly creeping fluids on geological timescales (Kaus, 2010; Thielmann and Kaus, 2012). The effect of melt on the viscosity is taken into account using laboratory-constrained creep laws (values are listed in Tables B3-B4 in Supplementary Data B). The numerical code, employed here, has been described in detail elsewhere (Kaus, 2010; Thielmann and Kaus, 2012; Johnson et al., 2014; Rummel et al., 2018) and is only briefly summarized here.

Governing equations The conservation of mass and momentum for slowly creeping incompressible rocks are described by:

$$\frac{\partial v_i}{\partial x_i} = 0 \tag{1}$$

$$-\frac{\partial P}{\partial x_i} + \frac{\partial \tau_{ij}}{\partial x_j} = -\rho g_i \tag{2}$$

where v is velocity, P = -0.5(σ_{xx} + σ_{zz}) is pressure, τ the deviatoric stress tensor, g is the gravitational acceleration, ρ is the density and i = (x, z) denotes spatial directions, and we employ a Boussinesq approximation.

The rheology is Maxwell visco-elasto-plastic:

$$\dot{\varepsilon}_{ij} = \dot{\varepsilon}_{ij}^{elastic} + \dot{\varepsilon}_{ij}^{viscous} + \dot{\varepsilon}_{ij}^{plastic} = \frac{1}{2G}\frac{D\tau_{ij}}{Dt} + \frac{1}{2\eta_{eff}}\tau_{ij} + \dot{\lambda}\frac{\partial Q}{\partial \sigma_{ij}} \tag{3}$$

where $\dot{\varepsilon}_{ij}$ is the (deviatoric) strain rate tensor, G the elastic shear modulus, $\frac{D\tau_{ij}}{Dt}$ the Jaumann objective derivative, $\dot{\lambda}$ the plastic multiplier and Q the plastic flow potential. η_{eff} is the effective creep viscosity, which is computed from dislocation and diffusion creep laws (Hirth and Kohlstedt, 2003):

$$\eta_{eff}^{dis} = FA^{-\frac{1}{n}}((C_{OH})^{r})^{-\frac{1}{n}}\ \dot{\varepsilon}_{II}^{\frac{1}{n}-1} exp\left(\frac{E+PV}{nRT}\right) exp\left(-\frac{\beta}{n}M\right) \quad (4)$$

$$\eta_{eff}^{diff} = FA^{-1}d^{p}((C_{OH})^{r})^{-1} exp\left(\frac{E+PV}{RT}\right) exp\ (-\beta M) \quad (5)$$

with F as prefactor for tensorial form, prefactor A, powerlaw exponent n, water fugacity in $H/10^6$ Si (C_{OH}), exponent of C_{OH}-term r, grain size d, exponent of the grain size p, second invariant of the strain rate tensor $\dot{\varepsilon}_{II}$, activation energy E, pressure P, activation volume V, gas constant R, temperature T, melt fraction prefactor β and M as current melt fraction. To avoid numerical instabilities, a lower and upper viscosity cut-off of 10^{17} and 10^{25} Pas is used.

The solved energy equation is given by:

$$\rho C_P\left(\frac{\partial T}{\partial t} + v_i\frac{\partial T}{\partial x_i}\right) = \frac{\partial}{\partial x_i}\left(k\frac{\partial T}{\partial x_i}\right) + H_r + H_a + H_d + H_l \quad (6)$$

where ρ is density, C_P heat capacity, $v_i\frac{\partial T}{\partial x_i}$ the advection term with v_i as spatial velocity and k is the thermal conductivity. H_r, H_a and H_d are the heat sources with radioactive (H_r), adiabatic (H_a) and dissipative or shear heating (H_d). Additionally, latent heat (H_l) induced by melting (heat consumption) or crystallization (heat production) processes is taken into account, by increasing/decreasing the effective heat capacity (C_{Peff}) and the effective thermal expansion (α_{eff}) of the partially molten/crystallized source, calculated following Burg and Gerya (2005) as:

$$C_{Peff} = C_P + Q_L \left(\frac{\partial M}{\partial T}\right)_{P=constant} \quad (7)$$

$$\alpha_{eff} = \alpha + \rho \frac{Q_L}{T} \left(\frac{\partial M}{\partial P}\right)_{T=constant} \quad (8)$$

with Q_L as latent heat of fusion. α_{eff} is considered in the adiabatic heating term H_a.

The density in the models is a function of rock composition (X), melt fraction (M), pressure (P) and temperature (T), with $\rho = f(X, M, P, T)$ and computed as follows:

$$\rho = \rho_{liquid} M + \rho_{solid}(1 - M) \quad (9)$$

where M is the current melt fraction and ρ_{liquid} and ρ_{solid} are the densities of the liquid and solid phase in equilibrium with the corresponding melt fraction.

In the following sections, we describe how the semi-analytical dike/sill formation algorithm and the phase diagrams are incorporated into the geodynamic code described above. We use different approaches for the sill emplacement (section "Mafic sill injection") and the dike formation (section "Formation of dikes").

Mafic sill injection

During the ongoing geodynamic simulation, basaltic magma is periodically injected (every 10-80 ka) as sills into different crustal levels. The intrusion depth and temperature are prescribed for each sill which is several km long. In addition to the predefined dimension of the sill (length and height), elasticity is crucial to calculate its spatial extension and its final shape. To describe how a fracture opens horizontally in an elastically deformable host rock, we use the analytical solution of Sun (1969) that defines the fracture/sill induced displacement of the host material (Ws) in a semi-infinite medium:

$$Ws = \frac{2iP_{sill}(1-\nu^2)}{\pi E_{ym}}\left\{z\ ln\left(\frac{R_2+z+ia}{R_1+z-ia}\right) - (R_2-R_1)\right. \tag{10}$$

$$\left. -\frac{1}{2(1-\nu)}\left[z\ ln\left(\frac{R_2+z+ia}{R_1+z-ia}\right) - iaz\left(\frac{1}{R_2}+\frac{1}{R_1}\right)\right]\right\}$$

where P_{sill} is the pressure within the injected sill, ν the Poisson's ratio, E_{ym} is the Young's modulus, a is the radius of the fracture (half of the sill length), R_1 and R_2 are complex distances and z represents the z-coordinate. $R_1 = \sqrt{r^2 + (z-ia)^2}$ and $R_2 = \sqrt{r^2 + (z+ia)^2}$ where r represents the radius of the polar coordinate system. i is the imaginary number $\sqrt{-1}$

$$P_{sill} = \frac{3E_{ym}V_{sill}}{16(1-\nu^2)a^3} \tag{11}$$

with V_{sill} as sill volume.

This fracture opening results in an elastic deformation of the surrounding rocks that is taken into account by moving markers. Within the horizontally-opened fracture, new markers are randomly inserted to mimic magma injection (see section “Injection and compaction of markers caused by melt extraction”). These markers carry the information (temperature, density, melt fraction, chemistry etc.) of the basaltic magma pulse by using a precomputed phase diagram. The injected sills provide a partially crystallized region as a source for further fracture generation to transport magma into shallower crustal depths (see section “Formation of dikes”).

Formation of dikes

The initiation and propagation of dikes are controlled by the interaction between mechanical stress-related processes and those that affect the magma behaviour (e.g., temperature and pressure). The stress field in the surrounding host rocks affects the dike which propagates in the direction of the maximum principal stress, σ_1. Moreover, the efficiency of magma transport

through a fracture depends on the fracture mode. Here, we apply a semi-analytical algorithm for crack initiation and propagation. The algorithm determines whether tensile fractures or shear bands would form around a partially molten/crystallized region, under the assumption that the magma pressure continuously increases in the source (Fig. 3). Only if tensile failure is favoured, is melt extracted from the source to fill the crack. We predefine the propagation direction of the crack using the local stress field. The dimension of the dikes is computed using the amount of extracted melt, within the constraints of the numerical resolution (see section "Size and orientation of dikes"). Apart from the mechanical evolution of the magmatic system, we track the chemical evolution in the deflated magma reservoir (after melt extraction) and in dikes by including changeable phase diagrams on the markers (Fig. 4). We extract pure melt from the partially molten/crystallized region assuming a total decoupling between melt and crystals either by forming local melt lenses in the mush system or by density-driven crystal settling (melt segregation). Although the melt fraction on each individual marker may be relatively small and thus normally not eruptible (Cashman et al., 2017), assuming perfect melt-solid separation allows us to extract melt as long as its amount is numerically resolvable on the mesh. After a sill is injected, dikes can only form in a subsequent numerical time step allowing melt accumulation through crystal-liquid separation.

The connected melt accumulations that trigger fracture initiation consist of melts originating from either one or several melt sources. These sources are not different rock types in the proper sense but are defined by the rock phase (e.g., crustal host rock, basaltic injected sill or dike). We tested two extreme scenarios, in which we assume i) full homogenization of all melts in the source region as long as these melts are connected, or ii) fully separated systems for melts from different sources, even if they physically coexist (immiscible melts). To mimic magma mixing, melt-carrying markers are randomly mixed from different sources (e.g. basaltic

sills and host rocks) such that a new melt extraction event would produce a dike which has both crustal and mantle signatures (Fig. 3; 4. Magma mixing).

From each generated dike of the first generation (formed from basaltic sills or from partially molten crustal host rocks), melt can be extracted again if either the material remains molten or enough heat is provided to partially remelt those rocks. These extracted melts form dikes of the second generation. Further melt extraction from dikes of the second generation is not allowed in our models. This limits the produced rock phases which is required to run the numerical code efficiently. Additionally, the used thermodynamic model is not suitable for higher evolved melts.

Determination of the failure mode above each melt accumulation The stress field and the critical pore fluid pressure (P_{crit}) above which the rock will fail, are determined for each element of the computational grid along the interface between the partially molten/crystallized source and the surrounded solid host rock. An analytical solution of the critical pore fluid pressure to induce failure in a porous elasto-plastic medium is given by Rozhko et al. (2007):

$$P_{crit} = \frac{k_b(\sigma_v - \sigma_h) + k_\tau + k_\sigma(\sigma_v + \sigma_h)}{k_f} \tag{12}$$

with σ_v as vertical effective stress (dynamic pressure (P) + deviatoric stress in the z-direction, σ_{zz}) and σ_h as horizontal effective stress (dynamic pressure (P) + deviatoric stress in the x-direction, σ_{xx}). k_b, k_τ, k_σ and k_f are constant coefficients (see Table B2 in Supplementary Data B) for various failure patterns (FM 1 – FM 4, described below). They are a function of the friction angle, cohesion, tensile strength and the two variables γ_σ and γ_τ which are described as follows:

$$\gamma_\sigma = 1 - \frac{\psi}{2}\frac{1-2\nu}{1-\nu}\left(1 - \frac{0.5}{ln\left(\frac{4h}{w}\right)}\right) \tag{13}$$

$$\gamma_\tau = \frac{\psi}{4}\frac{1-2\nu}{1-\nu}\frac{1}{ln\left(\frac{4h}{w}\right)} \quad (14)$$

with w defined as the width of the overpressure source (here, one element wide in order to numerically resolve it), h is the distance from the melt interface to the model top surface, ν is the Poisson's ratio, ψ is the Biot-Willis poro-elastic coupling constant.

The effect of fluid in the pore space is assumed to be negligible for the total stress in the host rocks. As soon as P_{crit} is exceeded, supposing an increase of the fluid pressure in the magma reservoir on top of the existing overpressure caused by the buoyancy of the magma, the rock will fail either by forming shear bands or tensile fractures (dikes). Four failure modes (FM 1 - FM 4) are defined by Rozhko et al. (2007), for which different equations are valid (see Table B2 in Supplementary Data B). Which of those modes are theoretically possible, depends on the local stress field (extensional vs. compressional conditions) along the melt interface. The minimal difference between the fluid pressure (P_{fluid}, dynamic pressure as a first approximation) and the critical pore fluid pressure (P_{crit}) indicates the failure position and the mode of failure (Fig. 3; 1. Failure mode and position; shear banding vs. tensile fracturing). Thus, only if P_{crit} is lower for the tensile fracturing than for the shear banding mode, is a dike formed. For a localized overpressure source, as applied here, equations of failure are rewritten as a function of parameters γ_σ and γ_τ, which affects both the shift of the Mohr's circle towards lower pressures and the size of the circle (Fig. 5). This increases, in our case, the critical pore-fluid pressure (P_{crit}) that has to be exceeded to initiate failure.

Size and orientation of dikes To generate a dike in our model, not only does the failure mode have to be favourable (tensile fracturing) above the partially molten/crystallized source (Fig. 3; 1. Failure mode and position), but also the amount of melt has to exceed a critical value.

The volume of magma (here assumed to be 100% melt) has to cover at least the dimension of two elements in both the *x*- and *y*-directions (ca. 200 m × 200 m) in order to be numerically resolved. However, only melt above the non-extractable amount (here set to 0.5 vol%) is extracted from the partially molten/crystallized region. The length of the resulting dike is computed from the extracted melt volume divided by the width of the dike, with a minimum width of two elements. As soon as the dike length exceeds the model dimension, the width increases by one element. With this simplification we focus on the processes below the Earth's surface neglecting magma fragmentation and the eruption itself. The orientation of the dike during its propagation is computed from the stress field in the model domain, such that it opens perpendicular to σ_1. To track the fracture propagation direction, fracture increments with a length of two elements are put on top of each other, under consideration of the local stress field, until the maximum length of the dike is reached, which depends on the available melt (Fig. 3; II. STAGE). The formation of each dike is accompanied by an elastic deformation of the surrounded host rocks, as described for the injected sills, but with a displacement vector that is constant along the dike (dike width does not change) such that the dike dimension reflects the volume of extracted melt.

Injection and compaction of markers caused by melt extraction After melt is extracted, markers are moved downward accordingly above the melt extraction zone to mimic the compaction of the deflated magma reservoir in a volume-conservative manner. This is a numerically simple manner to mimic volumetric processes within a Boussinesq model approximation. Other approaches are possible, which involve adding sink/source terms in the conservation of mass equation (e.g. Gerya and Yuen, 2007; Vogt et al., 2012; Schmeling and Arndt, 2017), but are not considered here. The formation of dikes causes an elastic deformation of the surrounding rocks. With the fracture opening, old markers are moved aside while new

markers are randomly inserted which carry the information about the rock properties (chemistry, density, etc.) of the newly generated dike (Fig. 3; 2. Compaction and injection of markers). The number of injected markers is equal to the number of markers that were located there before the fracture started to grow. The temperature within the newly formed dike is specified by the average temperature of the partially molten/crystallized source from which its melt was originated. The elastic deformation induced by the sill injection is strongest at the emplacement depth and decreases with increasing distance towards the surface and the bottom of the model box (eq. 10). Thus, the induced surface uplift can be relatively small if the intrusion depth is high. Therefore, the subsidence of crustal material caused by melt extraction can be larger than the uplift induced by the elastic deformation through the previous sill emplacement.

The procedure described is individually applied for each melt pocket. Parameters used for the geodynamic simulations including those for the dike/sill algorithm are listed in Table B5 in Supplementary Data B.

Phase diagrams employed in the geodynamic simulation

The computation of the phase diagrams used during the geodynamic simulation, can be done in two ways (i) by a direct call within the geodynamic simulation, or (ii) before the simulation for all previously requested rock compositions during compositional space investigation.

i) The computation of phase diagrams simultaneously with the geodynamic simulation allows us to reduce the number of computed phase diagrams of the database to a minimum, as all phase diagrams are based on the correct requested bulk rock compositions. After each melt extraction event, the residuum, cumulate or melt compositions are directly used to compute new phase relationships. The phase diagram

would be immediately updated on the marker, from which melt was extracted, and the chemical system develops accordingly. However, the disadvantage of this method is, that the geodynamic simulation has to wait until all phase diagrams are computed for each computational time step. The computation of each of those phase diagrams for a wide range in *P* and *T* takes in our case around 10 hours. Thus, even if the computation of the phase diagrams is executed in parallel, and only a single *P*-*T* point is considered, direct coupling is very inefficient, unless (future) major improvements are made to speed up the internal calculation time of the phase diagrams.

ii) To use precomputed diagrams requires a method to check whether a required phase diagram is already available. During an ongoing geodynamic simulation, the phase diagrams on the markers must be updated after the bulk rock compositions have been changed due to melt extraction (Fig. 3; 3. Update of phase diagrams). The affected bulk rock composition changes by splitting into a liquid part describing the extracted melt, and into a solid part to describe the remaining residuum (Fig. 4). To find the most appropriate phase diagram, we discretize the rock compositions with offsets of Δ_{Ox} = 0.1wt%. Thus, the chemistry of each marker is compared with an accuracy of one decimal to the already existing phase diagrams in the database. The phase diagram of the database, which has the closest bulk rock composition, replaces the previous one on the marker. Density, melt fraction and compositions are interpolated from the phase diagram to the markers. As soon as the phase diagrams are updated in the deflated magma reservoir, the rocks become depleted and thus acquire a higher solidus temperature. If a phase diagram with the requested bulk rock composition does not exist yet in the database, the rock composition is stored and will only be used after the geodynamic simulation has been completed to calculate a further phase diagram. The computation of those phase diagrams is executed in parallel to reduce the overall

computation time. However, updating marker compositions with the most similar bulk rock compositions during the geodynamic simulation may produce results that are chemically incorrect. Therefore, each geodynamic simulation has to be repeated, while computing new phase diagrams for the database, until the differences between requested and existing rock compositions in the phase diagram database are negligible. This can be verified by calculating a similarity index, D_{min}, which is a distance-based measure with units of wt% and denotes the Euclidean distance between every requested bulk rock composition ($BRC^{request}$) and its closest neighbour among all already existing bulk rock compositions used in the database (BRC^{dabase}).

$$D_{min,i} = \min_{j=1,\dots,N_{dabase}} \left(\sqrt{\sum_{ox=1}^{9} \left(BRC_{i,ox}^{request} - BRC_{j,ox}^{dabase} \right)^2} \right), i = 1, \dots, N_{request} \quad (15)$$

where *ox* represents the respective oxide and *N* is the number of rock compositions.

To avoid too many repetitions, the database is extended independently from the geodynamic simulation by defining new possibly needed rock compositions within the already existing compositional range. Even if not all of the phase diagrams are used in one specific geodynamic simulation, the large compositional range used in the database (with more than 58,000 bulk rock compositions) allows us to change the model setup without necessarily having to compute new phase diagrams.

The evolution of both the chemical composition and the melt fraction on the markers, which depends on temperature, magma mixing, and melt extraction, is graphically illustrated in Figure 4, without melt extraction (a) or with melt extraction (b).

Model setup

To better understand the dynamics and chemical differentiation of arc magmatic systems, we model a 50 km wide and 40-50 km deep 2D cross-section over ~1 million years (Fig. 6). The 2D model box consists of an upper, middle and lower crust, which are underlain by a pyrolitic mantle. We use a dry olivine rheology for the mantle and usually a quartzite rheology for the upper crust and a plagioclase (An75) rheology for middle and lower crust as well as for the sills and dikes (Table B3, see Supplementary Data B). We vary the rheology of the crustal host rocks in a few simulations to test the control of rheology on tensile fracture formation.

Mechanical boundary conditions are kinematic prescribed velocities on both model sides and on the bottom, where the velocity is chosen such that a constant extensional or compressional background strain rate of 10^{-15} s^{-1} is obtained (Fig. 6). For comparison, we also perform a simulation with no background deformation using free-slip boundary conditions. The top boundary is a free surface (stress-free). Thermal boundary conditions are isothermal at the top and bottom and flux-free at the side boundaries.

The initial geotherm has a surface temperature of 20 °C and increases linearly up to 600-800 °C at 40 km depth (14.5 or 19.5 ˚C/km) or up to 900 °C at 50 km depth. New basaltic magma pulses are periodically injected as sills (every 10-80 ka) into the continental crust or uppermost mantle at varying depth levels and lateral extensions (Fig. 6), with thicknesses between 0.5-3 km. Their injection conditions are prescribed. We choose sills as the igneous body geometry (separated ones or as amalgamation, Fig. 6; sills S1-S9) based on field observations (e.g., Torres del Paine intrusive complex, Leuthold et al., 2012). Other conceptual models of igneous body geometries exist as well, including a big magma tank, spherical or vertically elongated bodies and a funnel-shaped intrusion (Annen et al., 2015). We consider three different cases for basaltic magma intrusion: 1) sills are injected at constant depth into one main zone (single magmatic system), 2) sills are injected at constant depth into two main zones (double magmatic system, reference simulation), or 3) they are injected at variable depths

(non-connected). The intrusion temperature is set between 900 and 1200 °C, with 1050 °C as the most common one to simulate a mush-like starting system (with ~45 vol% crystals). The injection temperature of the basalt is constant during the geodynamic simulation for all sills. After ca. 400-500 ka, the heat and material influx from the mantle comes to an end and the magmatic system cools down.

RESULTS

In order to investigate the coupled petrological-geodynamical method outlined above, we systematically test a number of parameters and their influence on the mechanical and compositional evolution of the crustal magmatic system. For this, we change magma fluxes (sill injection frequency and the number of injections), sill-related parameters (such as size and temperature) and intrusion depths (upper, middle, lower crust or mantle; connected vs. unconnected sills). The effects of the initial state of the crust, such as geothermal gradient, mechanical boundary conditions (background strain rate) and the rheology of the host rocks, are additionally tested. Two different rock cohesion values (5 and 10 MPa) are used, as cohesion controls the fracture mechanism (tensile fractures vs. shear bands). Several hydration states of the initial crustal host rocks and injected basaltic sills are used (Table 1). The contamination of the mush system through assimilated host rocks is tested by including magma mixing in a simplified manner. The parameters used for the simulations are summarized in Table 2.

Reference simulation

Basaltic magma is periodically injected (36 times in total) into the middle and lower crust producing a new sill every 10 ka in the reference simulation (Fig. 7 and Table 2 model 19). These sills are injected in an extensional environment and have an initial thickness of 0.5 km each and an intrusion temperature of 1050 °C. The sill length is set between 10 and 17 km producing a volumetric magma flux of $3.9 \times 10^{-4} – 6.6 \times 10^{-4}$ km^3/km per year in our reference model (see values described in Annen et al., 2015). A rock cohesion of 10 MPa is employed, which causes dike formation as a direct consequence of a newly injected sill (no shear band formation). The melt produced at these conditions due to fractional crystallization (~50 vol% cumulate loss) has an intermediate rock composition. However, if further fractionation occurs by extracting residual phases from those partially crystallized dikes, high silica rocks can be generated. Towards the end of the simulation, dikes and sills form a complex and interacting network of differentiated rocks from crystallized melts, and their counterparts, the cumulates (Fig. 7). Through this dense network, heat is continuously released to the surrounding host rocks and triggers their partial melting (Fig. 7). However, some partially crystallized rocks maintain their original chemical composition if the system cools below the solidus temperature before the melt is extracted (Fig. 7, unmodified sill in light green and depleted sill in dark green in the zoomed-in area).

Dike generation and propagation and longevity of partially molten/crystallized regions

The extraction of melt depends on the stress field which controls the failure mechanism and thus the propagation of the dike (Fig. 8). Since fractures follow the orientation of the most compressive principal stress σ_1, dominantly horizontally propagating fractures are produced under compression, and dominantly vertically propagating fractures are produced under extension (Fig. 8). Locally, the far-field stress is disturbed by the generated dikes, injected

basaltic sills, or by subsiding overlying crust due to source rock compaction, through which uncommon fracture orientations may be produced. If there is no imposed tectonic deformation, the fracture propagation direction is usually between those observed under extensional and under compressional background strain rates. Furthermore, the rheology of the surrounding host rock influences the stress field and thus the propagation direction of dikes, e.g. a weak lower crust (wet quartzite, Table B3 in Supplementary Data B) generates very low differential stresses which results in the formation of non-vertically oriented dikes even with extensional background strain rates. For deeply rooted source regions in the uppermost mantle, efficient melt transport to shallower crustal levels is hampered due to a horizontal σ_1 orientation (model 16, Fig. 8).

We assume in all models a pressure in the partially molten/crystallized region that is sufficiently high to exceed the critical overpressure (P_{crit}, eq. 12) to break the rocks at any time. As long as sufficient melt is present, magma can be extracted to fill the opening tensile fractures. In most of the cases, after a sill is injected into the continental crust, the stress field above this partially crystallized region allows tensile fracturing and thus magma transport (see model 10, Fig. 9). The main controlling parameters on the failure mechanism, are the rock cohesion and the depth of the partially crystallized region. Using a smaller rock cohesion (5 MPa instead of 10 MPa) preferentially results in shear band formation. Consequently, dikes are not necessarily generated as a direct consequence of sill injection (models 7 and 26, Fig. 9), because the time of their formation only depends on the stress state of the surrounding rocks. This may result in the ongoing generation of late dikes from the early sills in a partially crystallized region which was not previously depleted by melt extraction. Therefore, even after the sill injection process is over (~400-500 ka), melt can still be present in a sill (Fig. 9).

In addition, the chosen depth of the injected sills influences the longevity of their partially crystallized regions (model 16, Fig. 9). The deeper the partially crystallized sill, the

less efficiently dikes are generated from it. Consequently, a magma reservoir in the lower crust (> 32 km depth) remains active by generating a stress field above the currently injected sills that preferentially results in the development of shear bands. This does not allow magma to be efficiently extracted. Using the modified failure equations (see eq. 13 and eq. 14) allows the formation of shear bands even under very low stresses in the lower crust. Dikes can be generated after the magma influx from the mantle has ceased due to the changing stress field, provided that sufficient melt is present.

Other parameters, such as the intrusion temperature, the initial thermal and mechanical state of the crust (rheology of host rocks, geothermal gradient, extensional vs. compressional environment), the number of injected sills (less thicker or more thinner ones) or the time at which they are injected, have no considerable control on the tensile fracture initiation. Even between single and double magmatic systems (one or two sill injection zones), or between connected (one injection depth) and non-connected sills (distribution of sills over a larger depth interval), there are no significant differences in terms of dike formation. Of course, partial melting of the host rocks may be influenced by those parameters as well, as e.g. a higher intrusion temperature heats up the surrounding material more efficiently, or specific dike/sill arrangements triggers host rock partial melting and thus potentially new dike formation. As long as melt is not extracted between different magma injections, the amount of melt decreases slowly due to diffusive cooling. This cooling process is faster for shallower reservoirs because of the higher temperature gradient to the surrounding material (models 7 and 26, Fig. 9).

To conclude, the first generation of dikes is normally triggered by the sill injection and only a lower rock cohesion or a deeper sill injection zone influences the fracturing mechanism in such a way that the magma reservoir remains partially crystallized despite waning magma influx from the mantle. Under these conditions melt extraction is not efficient and the melt fraction can only be reduced due to diffusive cooling. Thus, a deep magma

reservoir with a lower rock cohesion is the most efficient way to keep the system in a non-fully crystallized state (Fig. 9).

Chemical evolution of the magmatic system

The compositional evolution of crustal magmatic systems is investigated by tracking the rock composition on each individual marker. We visualize the rock compositional results on a TAS (total alkali-silica) diagram, in which different types of rocks are classified according to their SiO_2, Na_2O and K_2O concentrations (Fig. 10). Here, we use the classification of plutonic rocks after Middlemost (1994), in order to keep the rock names consistent over the whole modelled time independently of the melting/crystallization degree. Thus, the injected basaltic sills have a gabbroic composition, the upper and middle crust consist of granodiorite and the lower crust of gabbroic diorite. Starting from this gabbroic composition, the magmatic system evolves by fractionation as melt is extracted from the sill to fill tensile fractures (Fig. 10). The composition of these dikes is strongly affected by the degree of crystallization of the sill, from which the melt is extracted. Consequently, the elapsed time between a new mafic injection pulse and the extraction of melt is a crucial aspect. If the injected sills have an intrusion temperature of 1050 °C (~55 vol% of the material is initially liquid) and trigger directly the formation of tensile fractures, the generated dikes have a monzo-dioritic to monzonitic composition. Extracting melts from those dikes produces dikes of the second generation with monzonitic, syenitic/quartz-monzonitic or even granitic (with high Na_2O + K_2O concentrations) compositions (model 19, Fig. 10). Moreover, a deep-seated magma reservoir in the lower crust (~35 km depth) or in the uppermost mantle may also generate such high-silica enriched rocks (quartz-monzonite, granite, granodiorite; model 6, Fig. 10). These rocks are generated from small melt fractions (5-7 vol%) at temperatures < 850 ˚C. It is more difficult to generate tensile

fractures at these depths, which leads to melt retention in the partially crystallized region. Within this partially crystallized region, the temperature slowly decreases (if no fresh magma is locally injected) which results in an increase of the solid fraction, a related decrease of the melt fraction (Fig. 9), and thus an enrichment of the melt in both incompatible elements and silica content. Highly differentiated rocks can then be produced, if these melts (crystallization degree > 90% at ~850 ˚C) are extracted later, even though their source is basaltic in composition, leaving behind a mafic to ultramafic residue. Changing the rock cohesion from 10 MPa to 5 MPa has the same effect and diking is not favoured (model 26, Fig. 10). With a lower rock cohesion, the material fails due to shearing (Fig. 5b) where the magma extraction is not efficient. The remaining cumulates have a wide range in rock chemistry and are characterized by lower SiO_2 and $Na_2O + K_2O$ concentrations.

To conclude, in our simulations, highly silica-enriched rocks can be produced in several ways: 1) By retaining the melt in the sill, where it continuously crystallizes due to cooling (> 90% crystallizes, e.g. models 6 and 26), before being extracted; 2) By starting the mush-like system at lower initial temperatures, which reduces the amount of extractable melt; 3) By extracting residual phases from partially crystallized dikes (e.g. model 19); or 4) By melt extraction from partially molten host rocks (e.g. model 36). In all cases, the ratio between cumulates or residue and extracted melts controls the enrichment of the rocks, particularly the SiO_2 content.

If the temperature of intrusion is increased from 1050 °C to 1200 °C for deep crustal sills (initial melt fraction increases from ~55 vol% to ~82 vol%), the dikes formed from the extracted melts are slightly more mafic in composition compared to those generated at lower intrusion temperatures (Fig. 10 and Fig. A2, see Supplementary Data A). Since greater amounts of melt are extracted from the injected sills, their cumulates are slightly more depleted in SiO_2 (down to ~35 wt% in the TAS diagram) (Fig. A2, see Supplementary Data A). However, as

these sills are injected at deep crustal levels, even melts enriched in silica can be produced due to melt retention in the reservoir and therefore a wide spectrum in rock compositions is produced, from monzodiorite through monzonite to quartz monzonite and granite. Furthermore, due to the higher intrusion temperature, a larger amount of heat is provided to the surrounding, which produces granodioritic dikes from partially molten host rocks.

Mineralogical evolution of the magmatic system

In addition to the chemical composition, also the minerals are tracked on markers throughout the geodynamic simulation. This allows us to track the evolution of the mineral assemblages in time and space over the model domain (Fig. 11b). In order to visualize the mineral distribution within the magmatic system, we average the mineral concentrations over small domains. In these domains, the average mineral concentrations are shown on markers by allocating the respective mineral percentage to a number of markers with a specific colour. Thus, for example, if 60% consists of olivine and 40% of garnet, 60% of the markers have a green colour (for olivine) and 40% of them a red one (for garnet). The domains are defined for each coherent rock phase (e.g., crustal host rocks, basaltic injected sills or evolved dikes) and melt pocket. An example of mineral distribution is shown in Figure 11b for a geodynamic simulation after 450 ka (model 38). Exemplary mineral assemblages of that model are presented for different rock phases, dikes and cumulates below. The mineral assemblages are taken from the cooling magmatic system at sub-solidus conditions. Therefore, they show the equilibrium assemblage at a specific *P*-*T* condition and not necessarily the minerals which had been crystallized from the melt, so may include lower-grade metamorphic minerals that have overprinted the primary igneous ones. Dikes of the second generation, originating from the basaltic injected sills, are composed of mainly feldspar (~60%), chlorite (~17%), amphibole

(~15%), pyroxene (~6%) and minor Fe-stilpnomelane, quartz, biotite and spinel. Whereas, the cumulates of the first generation of dikes show a characteristic mineral assemblage consisting of: feldspar (~40%), amphibole (~30%), garnet (~15%), pyroxene (~10%) and minor olivine, biotite and spinel. Dikes of the second generation, but originating from the partially molten host rocks, have a higher proportion of felsic minerals, with: feldspar (~66%), quartz (~29%), amphibole (~2%) and minor mica and other accessory phases. Cumulates of the basaltic sills have mainly the following composition: feldspar (~42%), pyroxene (~30%), garnet (~14%), amphibole (~10%), ilmenite (~3%) and minor rutile (Fig. 11b, domain 4). All these mentioned mineral assemblages are only examples from that specific geodynamic model presented in Figure 11b and may vary over the model domain and with time.

Effect of magma mixing on fracture formation and chemistry

In order to test the effect of magma mixing on the evolution of the system, we perform simulations in which we employ a simplified magma mixing algorithm (Fig. 4). This algorithm allows us to mix magmas from different rock phases if they are contiguous. Thus, the magmas from the sills, dikes and partially molten host rocks can be mixed. This process reduces the total number of generated dikes but does not change the general mechanical behaviour. Nevertheless, through magma mixing, small accumulations of liquid (e.g., from the crustal host rocks) can be incorporated more easily into the active magmatic system, from which melt is continuously extracted.

The dikes follow the general trend as observed already for non-mixed magmas, from monzodiorite through monzonite to syenite/quartz monzonite or granite. Due to the mixing process, dikes from the first and second generation become indistinguishable. Contamination from the surrounding host rocks takes place at all crustal levels and is affected by their H_2O

content (models 30 and 45, Fig. 12). Under some conditions, more heat is provided to the host rocks through a dense dike and sill network. This allows a greater amount of newly-formed melt to be incorporated into the parental melts, or even to form separate dikes of predominantly locally-derived crustal partial melt towards the end of the active magmatic system. The magma mixing process produces in general rock compositions with a wider chemical spectrum. The melt chemistry from different reservoirs (sills or partially molten host rocks) merges which results in a greater diversity of cumulates left behind after melt extraction.

Influence of H_2O content on melting, host rock assimilation and dike formation

Low quantities of melt are extracted even from less hydrated crustal host rocks if the heat provided from the intruded dikes and sills is high enough (model 19, Fig. 13). Therefore, the intrusion temperature is an especially crucial parameter controlling the melting process of surrounding crustal material. However, the dikes derived from crustal host rocks are rare and generally limited to late extraction events (unless the intrusion temperature is increased). In Figure 13b we can see how the dikes temporally evolve, presented is the source of each dike (depth and origin, shown with squares), its volume (length of the dike) and its composition with a TAS diagram classification. However, the fact that melt was not extracted from the host rocks, does not necessarily imply that these rocks were not partially molten during the early stage of construction of the magmatic system. Thus, either the amount of melt was insufficient to be extracted (< 0.04 km^2 in our case for numerical resolution) or the fracture mechanism did not result in mode-1 dikes. Dikes from more hydrated host rocks are much more common and occur soon after the first sills were injected (model 38, Fig. 13b). In these hydrous host rocks, the initial H_2O content is increased to extreme values to see how the system changes if enough H_2O is provided, 5 wt% for the upper, 3 wt% for the middle and 0.5 wt% for the lower crust.

The dikes generated under these conditions are granitic or granodioritic in composition (Fig. 14). The compositions of the remaining depleted host rocks (or cumulates in dikes) range from peridotgabbro through gabbroic diorite/diorite to granite (Fig. 14). The partial melting of hydrated host rocks occurs throughout the modelled crust. A significant amount of melt can be accumulated, especially close to the cross-cutting network of sills and dikes, which provides a heat source to the surrounding material (Fig. 14). However, as long as the rock cohesion is ≥ 10 MPa, melt is nearly continuously extracted from the partially molten host rocks, limiting the lifetime of melt-rich areas between sill injection events to up to hundreds to a few thousands of years (model 38, Fig. 13).

As the melt-content increases in the host rock with increasing H_2O content, mixing between those melts with melts from basaltic sills or dikes, is enhanced (model 45, Fig. 12a). However, melt extraction from the basaltic sills is normally faster than heat diffusion, which does not allow significant host rock contamination (model 43, Fig. 12a). Therefore only at the sill margin, where melt was not previously extracted, small melt fractions remain and small-scale magma mixing leads to the formation of diverse rock compositions (model 43, Fig. 15). The melts from non-solidified dikes can be mixed to variable degrees with melts from newly injected sills and partially molten host rocks. For such a mixing event, we randomly redistribute all markers which carry a melt fraction and are located within the contiguous melting reservoir. The resulting dike compositions have a continuous mixing trend from monzodiorite to granite depending on the proportions of the respective melt phases.

Changing the H_2O content in the model for all basaltic injected sills (from 1 to 5 wt% H_2O; model 39, Fig. 13), increases the amount of initial melt from ~55 vol% to ~83 vol% with an intrusion temperature of 1050 °C. Dikes are generated as a direct consequence of a newly injected sill using a rock cohesion of 10 MPa. However, instead of producing multiple dikes from one injected sill, as it is observed for most of the other models (e.g., model 19, Fig. 13),

each injected sill generates only one dike by injecting a large amount of melt into the fracture (model 39, Fig. 13). The amount of injected melt per tensile fracture increases from the injected basalt with 1 wt% H_2O to the injected basalt with 5 wt% H_2O, from ~8 km^2 to ~11.5 km^2 (maximal amount), or ~3.9 km^2 to ~8.8 km^2 on average. Moreover, due to the greater amount of extracted melt, the residual rocks (cumulates) are more mafic and dikes are less chemically evolved with slightly lower SiO_2 and Na_2O+K_2O concentrations.

Decreasing the rock cohesion from 10 MPa to 5 MPa, stabilizes the melt containing reservoir (Fig. 15, model 44-45). Through this long-lived magma reservoir, a high amount of hydrated crustal host rocks can be assimilated through magma mixing or mingling (model 45, Fig. 12) and are accumulated due to density-driven convection if melt is not extracted (models 44-45, Fig. 15). Injecting basaltic sills at variable depth (deep middle and lower crust), with a surrounding rock cohesion of 5 MPa, is thus the most efficient way to keep the melt in the source (independently of the crustal H_2O content) by connecting the separated sills through melt driven convection (model 45, Fig. 15).

In Figure 12, the effects of rock cohesion and host rock H_2O content on the contamination process is illustrated. It is shown how much of the melt fraction originated from the injected sills is contaminated by melts from the crustal rocks. In models in which the rock cohesion is low (5 MPa), the size of the magma reservoir and thus the melt fraction continuously increases while host rocks are assimilated. The amount of the host rocks added to the mafic reservoir (sills and their dikes) through magma mixing increases with increasing crustal H_2O content from 1.50 km^3/km to 3 km^3/km at 490 ka (model 30 to model 45, Fig. 12a), which is an increase of the contamination percentage from ~6% to ~12%. If the rock cohesion is higher (10 MPa), melt extraction is more efficient and therefore the contamination is reduced even under H_2O-rich crustal conditions from 3 km^3/km to 0.6 km^3/km at 490 ka (model 45 to model 43, Fig. 12a), but the contamination percentage strongly increases in this case from

~12% to ~55%. This results from the fact that a single injected sill can heat up its immediate surrounding region such that a high amount of crustal melts can be assimilated into the mafic magma reservoir. If melts are extracted via dikes, the contamination of the magma reservoir is transferred into the dike phase (Fig. 12b). The average contamination percentage of the dikes is increased from 1.9 % to 7% by increasing the rock cohesion from 5 MPa to 10 MPa (from model 45 to 43, Fig. 12b), because although the total amount of melt is smaller for the second case, the dense dike-sill network delivers a significant amount of heat to the crust especially at lower crustal levels.

The width of a typical crustal partial melting zone is tens to a few hundreds of meters in distance to the sill margin as illustrated in Figure 16. The width of this zone is strongly affected by the composition of the host rocks (solidus temperature) and the injection temperature of the sill (Fig. 16). As the temperature decreases with time (if no heat is additionally provided), the affected zone narrows as well, but can also be enlarged if crustal material descends due to the deflation of the magma reservoir. In case magma mixing is involved, this zone describes the catchment area of the crustal contamination species.

DISCUSSION

In the following section, we discuss the model limitations, present the influence of different model parameters on melt extraction efficiency and thus on the chemical evolution of the solid and liquid fraction and show how our results can be used to better understand the dynamics of arc continental crust.

Model limitations and assumptions

We couple thermodynamic and geodynamic models by building a large database of precomputed phase diagrams that are used during geodynamic simulations. As soon as the rock chemistry changes on a marker due to melt extraction, the phase diagram with the closest bulk rock composition replaces the previous one. However, even with > 58,000 phase diagrams, rock compositions can still be produced during geodynamic simulations that are not closely represented by the bulk rock compositions included in the phase diagram database (e.g., the large variability of cumulate composition). In this case, the phase diagram database has to be extended and the geodynamic simulation must be repeated. Consequently, even if the pre-computation of the phase diagrams speeds up the geodynamic simulation itself, the required number of repetitions may slow down the overall process. Moreover, computing such a large number of phase diagrams automatically and in parallel does not allow us to visually inspect the results of all computed ones. Therefore, compositional artifacts in some phase diagrams are possible. Additionally, we use the solution models of Green et al. (2016) in Perple_X for the whole compositional range observed from the modelled sills, dikes and their residuum, yet the solution models are not perfectly calibrated for this full compositional range. The use of the more generalized model of Holland et al. (2018) in future may alleviate this potential issue. Using only simplified melt parameterizations, on the other hand, is also not advisable. The non-linear relationship between temperature and melt fraction shown on simple binary systems suggests that modelling of magmatic systems should be based on appropriate phase diagrams, which should account for different starting compositions (Caricchi and Blundy, 2015).

The evolution of a magmatic system is controlled by the interaction between chemical and mechanical processes, which is only incorporated in a simplified manner in our model. Ideally, a fully compressible formulation including three-phase flow and petrological reaction kinetics, that takes the change in magma properties during its propagation into account, is needed to solve everything in an internally-consistent way. We extract exclusively melt and

assume full melt segregation, even though this melt is still in equilibrium with the surrounding crystals until it is extracted. In nature, the fracture initiation and length scale of the dike is controlled by the stress and the failure conditions in the surrounding rocks, existing weak zones, change in magma overpressure, magma composition and density contrast between ascending magma and surrounding rocks, which are not or only partly considered in our model. The reason for this is that our numerical time step is much larger (hundreds of thousands of years) than the average crustal transport rates for mantle magmas (80 m per day, Ruprecht and Plank, 2013). As it is widely recognized that fractures can efficiently transport granitic magmas through the crust (e.g. Clemens and Mawer, 1992; Petford et al., 1993), we exclusively allow our melt to be transported through tensile fractures. At shallower crustal levels, non-solidified felsic dikes/sills may interact in our models, or even coalesce to form larger plutonic bodies (Clemens and Mawer, 1992). Stress release through either melt flow along grain boundaries into the surrounding crustal rocks, shear band formation, or volume change due to crystallizing magma, is not taking into account. Thus, we assume that the pressure in the partially molten/crystallized source is sufficiently high to break the rocks due to melt segregation through compaction, or through mafic refill from below. Furthermore, the solidification of the modelled dikes is slowed down due to their thickness defined by the numerical resolution. In nature, thin dikes/sills cool much faster. However, if several thin dikes are emplaced in a narrow zone, the average temperature is kept high, preserving them in a partially crystallized state. Therefore, within dike swarms in the lower crust, partial melting of crustal material and magma mixing and mingling processes are most efficient (Dufek and Bergantz, 2005). This is consistent with our models, in which the heat supply from densely distributed dikes/sills leads to intensive crustal partial melting, especially for hydrated host rocks (Fig. 11 and Fig. 14), and contamination from them (Fig. 15). Even though different magmas may not mix due to their viscosity contrast, which is not considered in our simplified mixing model, magma mingling

may potentially take place. Considering our numerical resolution (between 2 and up to 10,000 markers in each grid cell), magma compositions can be averaged independently of the dominant magmatic process (magma mixing or mingling), because magma mingling may take place in nature on much smaller scales (millimeters to meters). If the minimum or maximum number of markers is reached per grid cell, markers are added or removed in our model. Furthermore, we inject sills as opening fractures in elastically deformable host rocks, even though viscous behaviour could play an important role as well, especially for the deep injection zones. Here, mafic influx warms up the surrounding continental crust, which may influence the storage behaviour (Karlstrom et al., 2017). However, in general, the viscosity contrast between the injected basalt and solid rocks is sufficiently high, and timescale of emplacement in nature sufficiently short to promote elasto-plastic fracture formation (Rubin, 1993).

Eruptible, liquid-dominated bodies, can form within a mush through fractional crystallization. The melt fraction window of 30-50 vol% is most favourable for liquid-crystal separation (Dufek and Bachmann, 2010). This may rapidly localize melt lenses in our model after a new sill is injected with ~55 vol% melt with an intrusion temperature of 1050 °C. Furthermore, melt can be accumulated due to compaction-driven melt segregation, which under low melt fractions is strongly controlled by the melt viscosity and matrix properties (McKenzie, 1984). For the spatial dimension of our modelled single sill (usually ~1 km thick), compaction of the solid matrix seems to be a powerful mechanism to squeeze out the melt fraction and thus to accumulate a high amount of melt within a short time, comparable with our employed numerical time step of few hundreds of years (Tegner et al., 2009). This justifies the assumption of the extraction of pure liquid in our model.

Within the assumptions or simplifications made here, our results show some first order mechanical effects on the chemical evolution of magmatic systems and illustrate that we can track the evolving chemistry in time and space with a high degree of precision.

Maintenance of a magma reservoir and its implication on magma chemistry

Influence of model parameters on the longevity of the reservoir and magma chemistry

The chemistry of the extracted melt and cumulates/residuum depends on the chosen starting conditions and the evolution of the magmatic system. The initial bulk rock compositions (for basalt and host rocks) affect magma differentiation processes, and injection conditions of the sills and crustal depths control the first melt fractions and their chemical compositions (Fig. 10 and Fig. A2, Supplementary Data A). In case melt is not immediately extracted from the magma reservoir via dikes, other parameters such as the geothermal gradient become important (Fig. 9). The failure mechanism is exclusively controlled in our models by the stress field above the magma reservoir and the rock cohesion which both affect the melt extraction efficiency such that a higher rock cohesion (≥ 10 MPa) or shallower crustal magma reservoirs facilitate diking (e.g. Figs. 9-10). Magma mixing can further influence the longevity of the system (Fig. 15). Chemically evolved magmas from the crust or previously generated dikes can be mixed with more mafic ones from the intruded sills that cools down the common magma reservoir if those evolved melts exist at lower temperature conditions. However, this process may also maintain the reservoir in a non-fully solid state until new mantle magma is emplaced (Fig. 15). Therefore, our models indicate that the evolving chemistry is the main controlling parameter in maintaining the system in a partially molten/crystallized state, instead of the heat supply alone as suggested in previous studies (e.g., Annen et al., 2015). However, successive melt extraction can also deplete the source region. Therefore, even if the temperature is relatively high, the melting/crystallization degree is strongly affected by the composition of the rocks that controls the solidus temperature, and which changes as soon as melt is extracted (Fig. 2c). The

modelled cumulates left behind after melt extraction can have a wide spectrum in chemistry depending on how much melt was extracted from different stages of the system evolution (Fig. 10, Fig. 14 and Fig. A2 in Supplementary Data A). Cumulates from the sills have mainly a gabbroic to an olivine-gabbroic composition, but they can even be more depleted if a greater amount of melt was extracted (e.g. for models with a higher H_2O content in the basalt or with a higher intrusion temperature; Fig. A2 in Supplementary Data A). The largest volumetric contamination of the magma reservoir is reached for a long-lived magmatic system that is surrounded by a strongly hydrated crust (Fig. 12), but the contamination per each individual sill in a densely distributed dike-sill network can be higher in short-lived magmatic systems (Fig. 12).

How can we form highly differentiated melts?

The enrichment of extracted melts is controlled by the solid-liquid ratio which is influenced by the reservoir evolution (Fig. 17a). If no heat is added through a new mafic magma intrusion, the solid-liquid ratio increases in a cooling magma reservoir which changes the chemistry of the melt and of the solid fraction as shown in Figure 17a. Starting with a partially crystallized zone composed of injected sills, with up to 50 vol% melt fraction, the composition of the melts evolves with decreasing temperature from monzodiorite to granite (black-filled circles, Figure 17a) following the liquid lines of descent of igneous natural rock suites. From different cooling stages and thus crystallization degrees, melts can be extracted to form dikes (extracted melt compositions are presented as orange-filled circles, Fig. 17a). Investigating the compositions of dikes formed within all executed geodynamic simulations suggests a clear trend between the SiO_2 content and the crystallization degree of the source (Fig. 17b), the higher the crystallization degree the higher the SiO_2 concentration. Exceptions are dikes originating from

partially molten host rocks, which already have a high SiO_2 concentration independent of the melting degree (Host rock melting, Fig. 17b), since those rocks are already highly enriched in incompatible elements. The residuum of the crustal rocks can be highly depleted (down to 40 wt% SiO_2, Fig. 14).

Experimental studies show that in order to produce rocks with a rhyolitic composition, the parental magma of basaltic composition has to be crystallized by at least 80%, whereas the formation of andesitic-dacitic melts requires only a crystallization degree of 40-60% (Sisson et al., 2005; Scaillet et al., 2016). A rhyolitic liquid can form at near-solidus conditions by advanced crystallization-differentiation of a mantle-derived basaltic source (e.g. Sisson et al., 2005; Ulmer et al., 2018; Müntener and Ulmer, 2018; Jagoutz and Klein, 2018). Other authors suggest that the crystallization of basaltic magmas in combination with host rock melting generates silicic magmas, forming a mobile magma through melt segregation in the mush (Solano et al., 2012, 2014; Riel et al., 2018). Our model results show that a relatively cool mush system (high crystallization degree with > 90% crystals, Fig. 10) may form silicic rocks from a primary basaltic bulk rock composition, but also magma mixing can shift the melt compositions towards rhyolites/granites, as melts generated by the host rocks have a rhyolitic to granodioritic composition (Figs. 10 and 14). Additionally, rhyolites may also form in dikes of the second generation through fractionation of basaltic magma (Fig. 10).

In our models, most of the melt extraction is triggered by mafic influx from below, producing only relatively small eruptive volumes proportional to the volume of the previously injected basaltic sill (Fig. 7). Under particular model conditions (deep sill injection zone or low rock cohesion, Fig. 9), the melt may stay in the magma reservoir, where it can fractionate and differentiate to more highly evolved rocks (e.g. Annen et al., 2015). Magma reservoirs in the lower crust remain active for a long time, forming a zone in which melting, assimilation, storage (fractionation), and homogenization (magma mixing) (MASH, after Hildreth and

Moorbath, 1988) take place. In addition to those processes, remelting, recharge and magma eruption are further aspects that control the chemical and the mechanical evolution of magmatic systems. The efficiency of melt extraction from the reservoir is a crucial factor in maintaining a larger mush zone. This partially crystallized zone is formed either through a merging of formerly separated partially crystallized sills (model 45, Fig. 15) or through a heat addition due to the injection of fresh basaltic magma into the already existing mush zone (model 44, Fig. 15). Older undepleted material (injected before as basaltic sills, now crystallized) can even be reactivated through the heat supply of a new basaltic influx. Younger magma pulses may be efficient in recycling of older plutonic material (e.g. Paterson et al., 2008) resulting in extensive mixing of crystals and melts. However, the total amount of eruptible melt is not necessarily correlated with the size of the magma reservoir, because it is controlled by the crystallization degree that increases with decreasing temperature. Thus, if melts accumulate over a large area, a large eruptible melt volume can be produced (Fig. 12a), despite a high average crystallization degree. This may, on the long term, result in episodic events of eruption of highly differentiated liquids (Fig. 10). This is consistent with geophysical observations suggesting that the failure to find large bodies of fully molten magmas likely requires the existence of large mush bodies with only small melt fractions (e.g. Pritchard and Gregg, 2016; Novoa et al., 2019).

Stratification of arc continental crust

Relative importance of generated rocks

To evaluate the importance of the different modelled rock phases (sills, dikes, host rocks, cumulates and residuum), we calculated their volumes, compositions and average densities for given SiO_2 concentrations. The total amount of newly-created crust is dominated by the

injected basaltic sills, followed by dikes which were generated from them. The volume ratio between injected sills and dikes of the first and the second generation is influenced by the melt extraction efficiency that controls the ratio between the remaining cumulates and the amount of extracted melt. The newly-created crust can nearly exclusively consist of basalts using a low rock cohesion of 5 MPa (model 26, Fig. 18). Partial melting of host rocks modifies the crustal composition only to a minor extent and is only relevant for a strongly hydrated primary crust (model 38, Fig. 18). Using this hydrated crust (upper crust: 5 wt%; middle crust: 3 wt%; lower crust: 0.5 wt% H_2O, Table 1), the volume of rocks highly enriched in silica (> 70 wt% SiO_2) increases, which is small under lower crustal H_2O contents and normally dominated by the fractionated magma from the sills (dikes of the second generation). The volume ratio between fractionated melts from the sills and those generated during crustal partial melting strongly decreases from ~49 to ~4 from model 19 (reference simulation) to model 38 with increasing crustal H_2O content (Fig. 18). However, this ratio is much smaller if only the felsic rock production is considered. For model 38, the ratio decreases from ~4 (~10 km^3/km fractionated magma from crust and ~45 km^3/km from sills for all SiO_2 concentrations) to ~0.35 (~10 km^3/km fractionated magma from crust and ~3.5 km^3/km from sills with SiO_2 > 66 wt%). For model 19 the same trend is observed and the ratio decreases from 49 (~0.5 km^3/km fractionated magma from crust and ~25 km^3/km from sills for all SiO_2 concentrations) to 17 (~0.5 km^3/km fractionated magma from crust and ~9 km^3/km from sills with SiO_2 > 66 wt%). Consequently, fractional crystallization from basaltic sills is the main mechanism to produce intermediate rock compositions and is only to a minor extent responsible for felsic rock production. As the crust produces by default already such highly evolved rocks in our models (Fig. 17b and Fig. 18), is its contribution to felsic rocks mainly controlled by its melt fraction influenced by the H_2O content.

The silica concentration of the sill-cumulates changes with depth, temperature and bulk rock composition of the injected sill. Low SiO_2 concentrations are produced in the cumulates either under shallow injection depths assuming constant intrusion temperatures, with high intrusion temperatures, or with a hydrated initial basaltic composition (Fig. 18 and Fig. A3, see Supplementary Data A). In contrast, a high SiO_2 concentration in the cumulates requires a deep sill injection zone (model 6, Fig. 18) or lower intrusion temperatures. All these parameters influence the crystallization degree, such that a lower silica concentration implies a greater amount of extracted melt. The modelled dikes become more enriched in silica through melt retention in the source (increased degree of crystallization). However, not only the melt extraction efficiency but also the temperature that keeps the system in a partially molten/crystallized state and the pressure conditions (as melt fraction changes with pressure at constant temperature) are crucial for the evolution of the dike chemistry.

The density of the rocks decreases in general with increasing silica content in our models (Fig. 18). The basalt injected as sills into the crust, has, in a fully crystallized state, a higher density (3035 kg/m^3 with 1 wt% H_2O or 2960 kg/m^3 with 5 wt% H_2O) than both the upper (2823 kg/m^3 with 1 wt% H_2O or 2639 kg/m^3 with 5 wt% H_2O) and the middle crust (2849 kg/m^3 with 0.5 wt% H_2O or 2791 kg/m^3 with 3 wt% H_2O), and a lower density than the lower crust (3127 kg/m^3 with 0.1 wt% H_2O or 3071 kg/m^3 with 0.5 wt% H_2O). Consequently, delamination of basaltic material into the lower crust or mantle is not possible using the chosen basaltic and crustal rock compositions. However, if melt is extracted, the remaining cumulates can be denser than the surrounding crust and the underlying mantle (Fig. 18 and Fig. A3, see Supplementary Data A). This can lead to delamination of dense cumulitic material into the deep lower crust (lingering at the Moho) or even into the mantle, on the long term, and may explain the paradox between the volume of silicic magma and that of the remaining cumulates. The observed volume of mafic-ultramafic cumulates in exposed crustal arc sections is far too

low to explain large granitic bodies through fractional crystallization of a parental mafic melt. Therefore, delamination of dense cumulitic material is suggested (e.g. Jagoutz and Kelemen, 2015; Jagoutz and Klein, 2018). Using a hydrated mantle (not modelled here) and a more hydrated lower crust may also favour this process by lowering both their density and their viscosity.

Comparison with igneous rocks in arc settings

An arc system is dominated by igneous rocks and their cumulates. Exposed crustal sections show a continuum from mafic cumulates (indicating mineral accumulation and melt loss) to felsic intrusives (frozen liquids) in the upper crust, and indicate that most magmatic differentiation is restricted to the lower crust (Jagoutz, 2014) as shown also in our models (Fig. 9). In this section, we compare magmatic rocks generated in our models with igneous rocks from the Kohistan and Famatinian arc exposed sections. The Kohistan arc is located in NW Pakistan and represents a fossil Jurassic to Cretaceous island arc that was wedged between the Indian and the Asian plates during their collision. It consists of the Southern Plutonic Complex (SPC), the Chilas- and the Gilgit Complex (e.g. Jagoutz et al., 2011). The SPC represents the upper mantle and the lower to middle crust of this island arc and shows a cumulate sequence formed by “hydrous” medium- to high-pressure fractionation (Jagoutz et al., 2011). The Chilas Complex is a large ultramafic-mafic intrusion and its magmatic sequence is suggested to result from “dry” lower crustal fractionation (Jagoutz et al., 2011). The Sierra Valle Fértil represents a lower to middle crustal section of the Early Ordovician active margin of West Gondwana, the Famatinian arc, which is located in central-western Argentina (e.g. Otamendi et al., 2010a, 2012; Walker Jr et al., 2015). Our modelled compositions are similar to the igneous rocks observed in the Kohistan and Famatinian arc (Fig. 19). Differences in the magmatic and

cumulate/residual rocks trends are mainly observed for the MgO- and TiO_2 content. The MgO concentration is higher for some samples of the Kohistan arc compared to the modelled rock compositions and the TiO_2 concentration can be higher in the modelled cumulates (Fig. 19). The thermodynamic melting model does not incorporate Ti that is why all Ti can be stored in ilmenite and rutile, in our models. The high MgO concentration comes from mantle rocks (peridotites) absent in our model compositions. Other differences between modelled and natural igneous rocks are potentially a consequence of the chosen initial basaltic composition, the oxygen fugacity that controls the Fe^{2+} to Fe^{3+} ratio, intrusion and melt extraction conditions and constraints of the thermodynamic model. Furthermore, the composition of partially molten and thus assimilated host rocks and pervasive melt flow (e.g., Riel et al., 2018) may influence magma compositions as well within each specific case study.

Significance of the models

The integrated-thermodynamic-geodynamic models presented here extend our knowledge about crustal magmatic processes, as our new approach allows us to constrain how the chemistry and melt fraction change throughout the continental crust. The study of such magmatic dynamics over space and time is generally limited by the accessibility of exposed rocks. Here, we show how key parameters influence the volume and diversity of magmatic rock types which may have a significant long-term influence on the gravitational stability of the crust. In future, our code could be used to quantify the contributions of different processes (fractionation vs. magma mixing, source of the melt, melting conditions etc.) to the formation of natural arcs and the spatial distribution of different igneous rock types within an active subduction setting. However, comparing model results with natural observations remains

always challenging, as each of the neglected processes may have a large influence on the whole evolution of the magmatic system.

CONCLUSION

We studied the chemical and mineralogical evolution of arc-related crustal magmatism by integrating thermodynamic models into a visco-elasto-plastic geodynamic code. The compositional evolution consisting of 10 major oxides, is tracked on more than a million markers, while recently developed thermodynamic models for metabasic rocks (Green et al., 2016) are employed to simulate melting and crystallization. As the chemistry continuously changes as a result of melt extraction, new thermodynamic computations are continuously required. To make this computational tractable, we developed a system which links geodynamic models with over 58,000 precomputed phase diagrams that allows tracking the temporal evolution of the evolving rock chemistry and mineralogy as well as its feedback on the mechanics. Magma mixing and the effect of host rock contamination can be included in a simplified manner as well. The geodynamic simulations are linked with a simplified parameterized semi-analytical dike and sill formation algorithm, which tracks whether mode-1 cracks (fluid-filled dikes) or mode-2 shear zones may develop as a result of melt pressure and local stress state. Dikes drain the partially crystallized mush chambers and propagate perpendicular to the main compressive stresses, with a size that depends on the amount of available melt.

With this modelling approach, we can test the chemical, mechanical and thermal evolution of a crustal-scale magmatic system, as a function of tectonic deformation, magma fluxes and sill-related parameters (such as size and temperature). We performed systematic

numerical simulations to better understand the physics of this system and the main findings are:

1) Sill injection can often immediately trigger dike formation, unless the cohesion of the host rocks is sufficient low (< 10 MPa) and/or the sills are emplaced sufficiently deep (> 32 km). In cases rocks cohesion is low enough or injection depth deep enough, longer-lived mush bodies are formed over hundreds of thousands of years. The size of those bodies correlates initially with the injection area of the sills but decreases with time as the system cools down.

2) Partial melting of crustal host rocks occurs in areas with densely distributed dikes and sills. A higher sill intrusion temperature (1200 ˚C) or a higher H_2O content in the host rocks (up to 5 wt%, 3 wt% and 0.5 wt% in the respective crustal sections) promote partial melting of the host rock and contamination of mantle-derived magmatic sills. The width of the partially molten zone is between tens of meters and up to few hundreds of meters.

3) The composition of the newly-created igneous rocks varies between peridotgabbro (or even more depleted) for cumulates and highly differentiated rocks like syenite, quartz monzonite or granite for dikes. Fractionation trends of the modelled magmatic rocks are consistent with those observed in the Kohistan and Famatinian arc.

4) Highly-differentiated rocks such as granites can be formed by i) continuous melt extraction from previously generated dikes, ii) crustal host rock melting, or iii) high-degree crystallization of basaltic sills. To increase the crystallization degree, either the intrusion temperature has to be decreased (starting with a colder mush system) or the magma reservoir has to live longer (see point 1).

5) Magma mixing generates a wider spectrum of rock compositions having both a crustal and a basaltic sill component in dikes and cumulates in different proportions.

Partially molten (wet) host rocks can be assimilated by mixing or mingling processes into the magma reservoir.

These results thus show that mechanical and chemical processes interact and that both of them must be considered to model natural magmatic systems. To a first order, our results are consistent with existing models of deep magma reservoirs that maintain active for a long time (a hundred thousands of years) forming a zone in which fractionation, assimilation, and magma mixing occur. However, it is not temperature variations that primarily controls the maintenance of the partially molten/crystallized region, but the change in solidus temperature as a function of rock chemistry change driven by open system processes.

ACKNOWLEDGEMENTS

We would like to thank the ZDV at the University of Mainz to provide us computational time on MOGON I cluster to run Perple_X in parallel. We would like to thank the Editor Wendy Bohrson and the reviewers Luca Caricchi and Muriel Gerbault for the useful comments which massively improve the paper.

FUNDING

Funding was provided by the VAMOS Research Center, University of Mainz (Germany) and by the ERC Consolidator Grant MAGMA (project #771143).

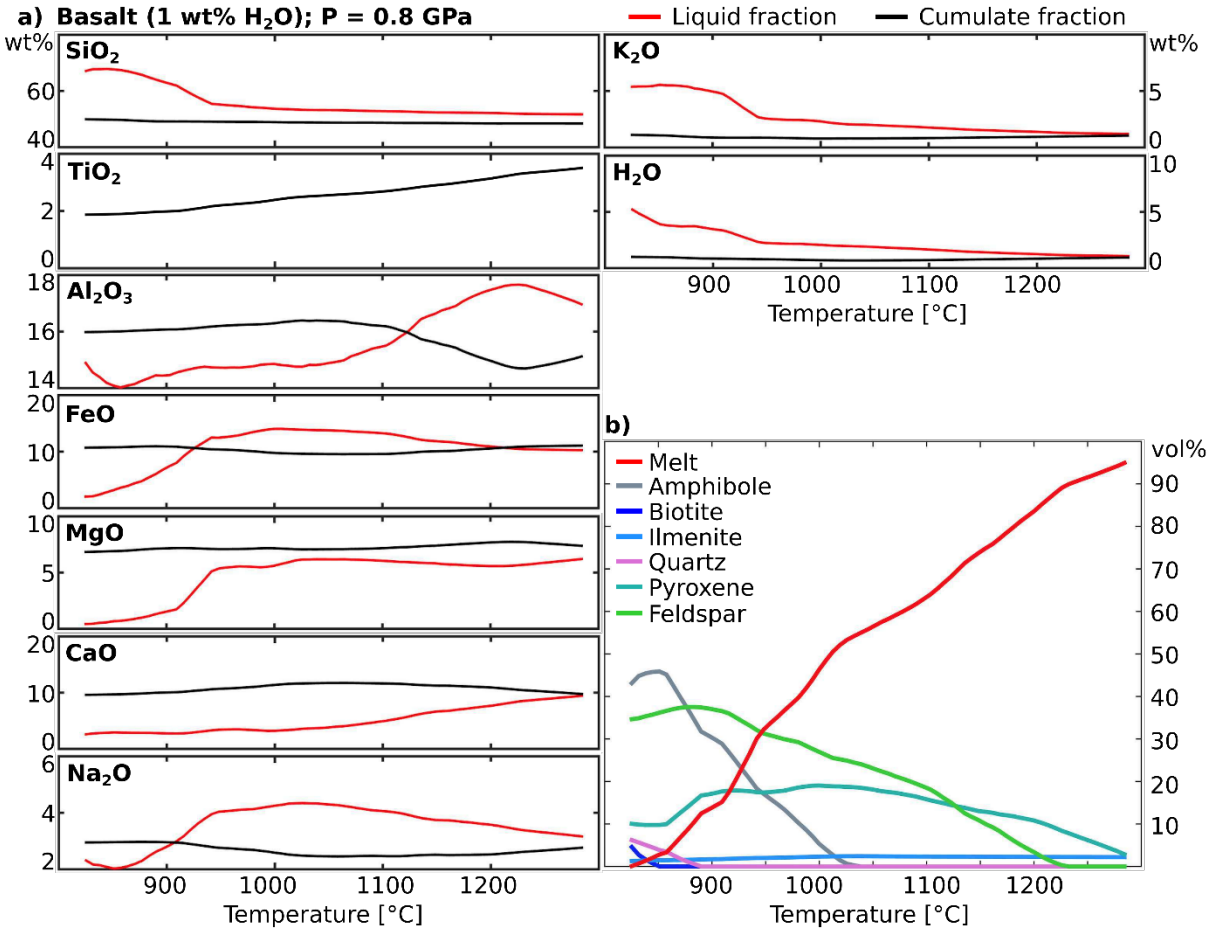

Fig. 1. a) Chemical evolution of melt and cumulate (solid) fraction of the basalt (with 1 wt% H_2O, see Table 1) with increasing temperatures (P = 0.8 GPa). b) Phase evolution with increasing temperatures (P = 0.8 GPa).

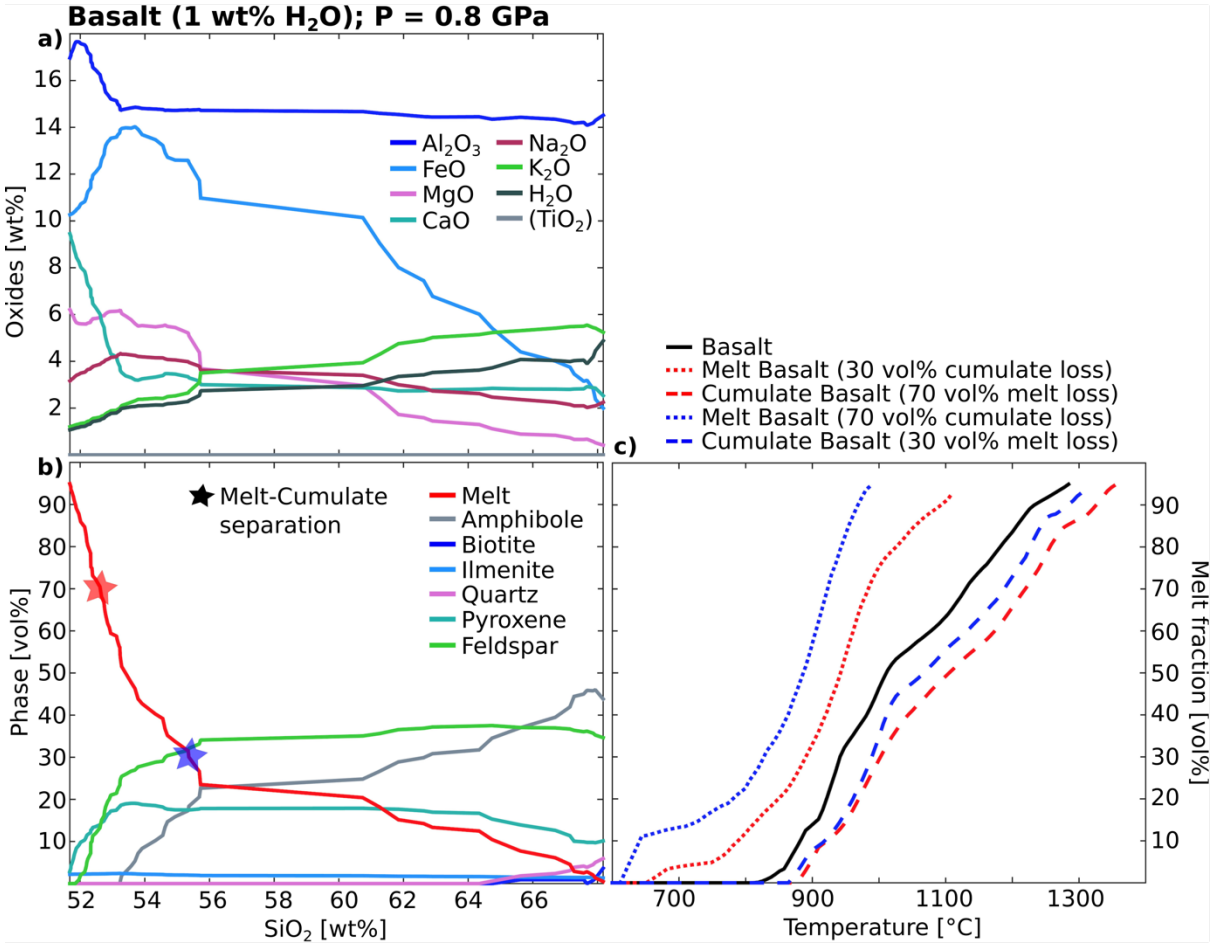

Fig. 2. Oxide evolution (a) and phase evolution (b) with increasing SiO_2 concentration of the basalt with 1 wt% H_2O (see Table 1) at P = 0.8 GPa. Melt is extracted from different melting degrees (30% crystal loss = red star and 70% crystal loss = blue star). c) Change of melt fraction with temperature for the initial basalt (black line) and for the two cumulate and melt compositions generated at the different melting degrees (red and blue stars).

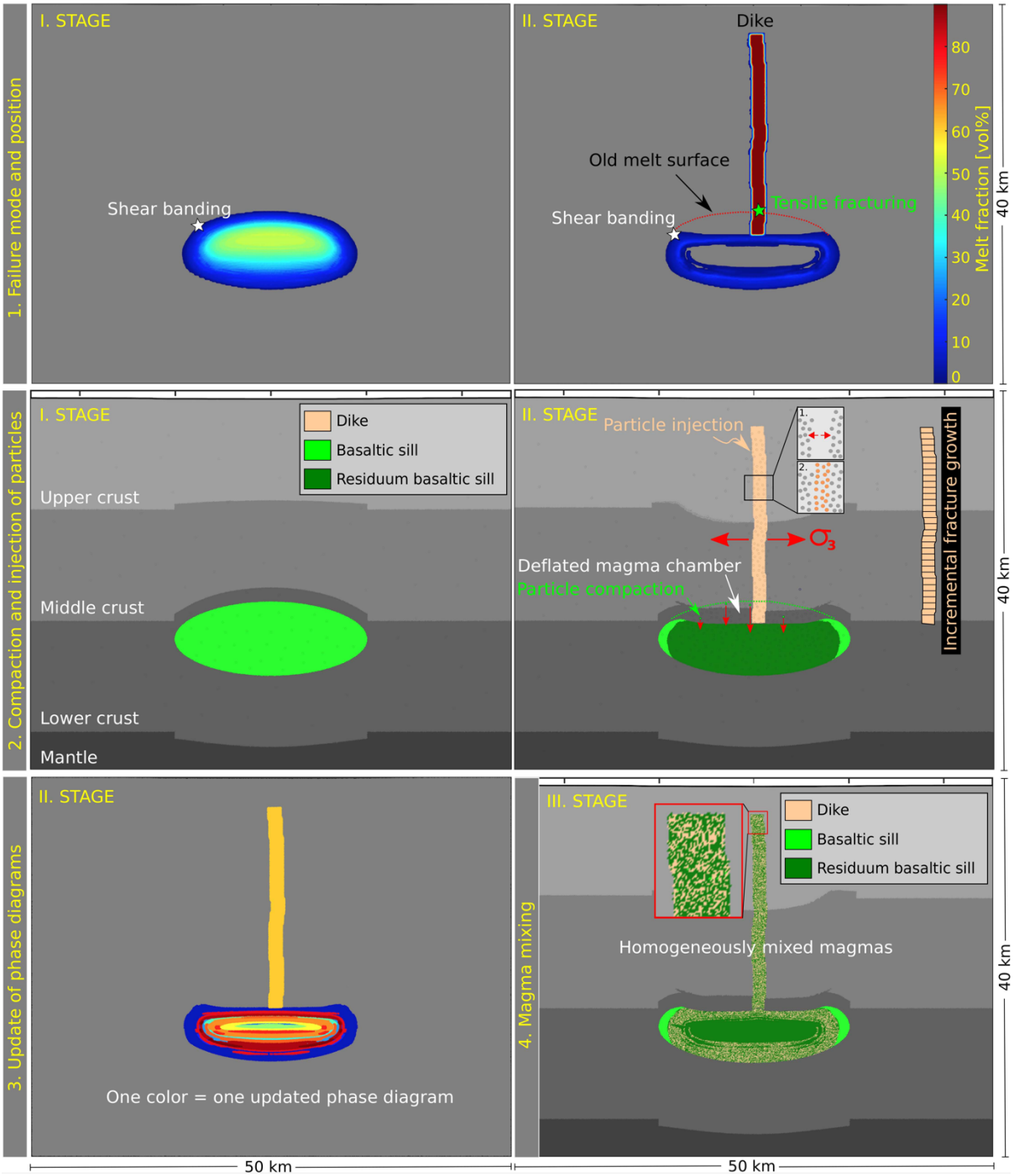

Fig. 3. Methodological procedure of melt extraction 1-3, with magma mixing (4) as a potential additional step. Stages I to III represent the temporal sequence. Stage I: Magma reservoir is stable and the stress field only favours shear band formation above the partially crystallized region. Stage II: magma reservoir becomes unstable and a tensile fracture is formed. The fracture incrementally propagates in σ_1 direction. Melt is extracted from the magma reservoir into the fracture to form a dike. Subsequently, the markers are compacted in the deflating magma reservoir and around the fracture. Injection of markers into the newly formed fracture that carry the information of the melt phase. The phase diagrams used are updated based on the cumulate and melt chemistry. Stage III: Magma is mixed between different connected sources by mixing their melt-carrying markers (orange markers for the melt of the dike and green markers for the melt from the sill).

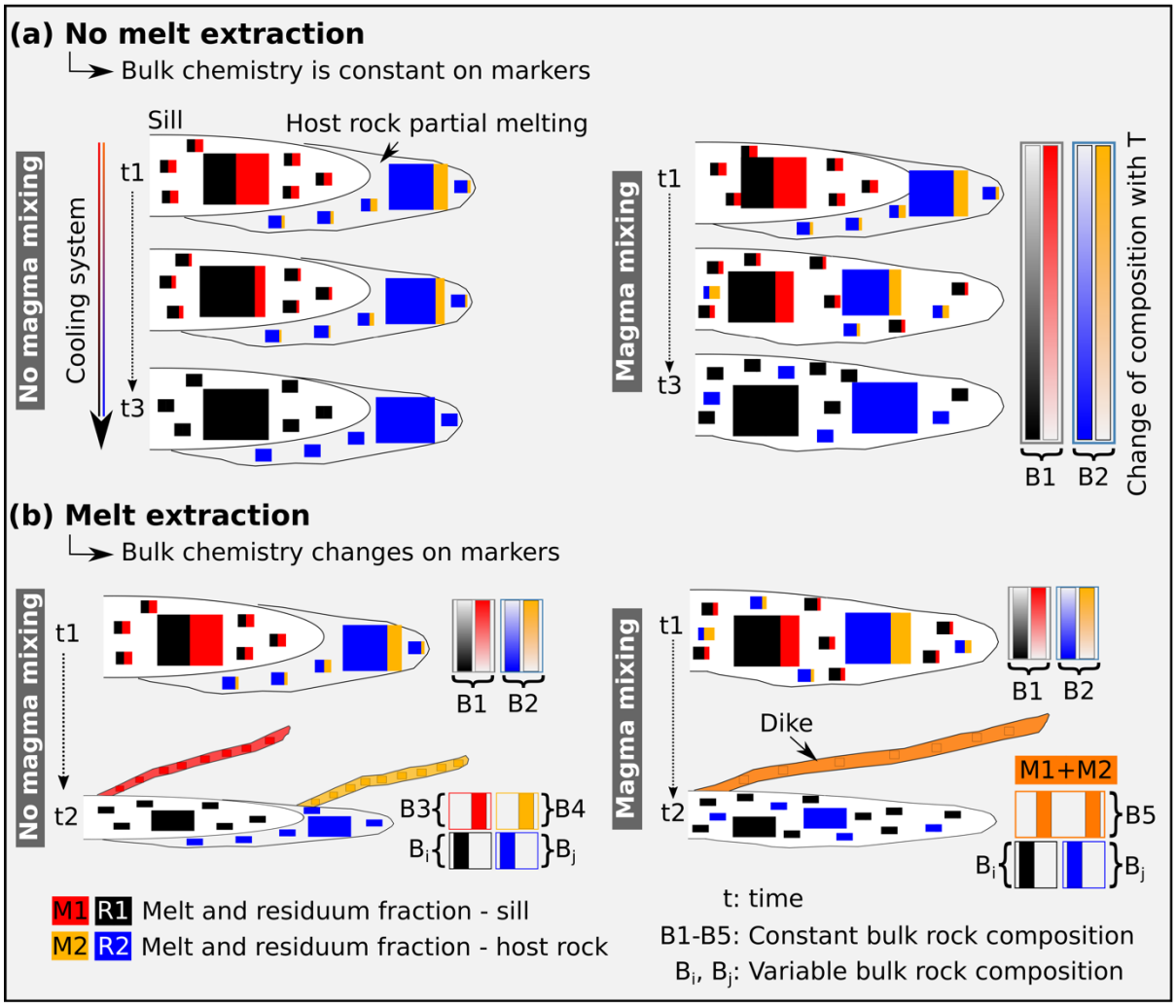

Fig. 4. Scheme describing the evolution of chemistry and melt fraction. a) Melt is not extracted from a sill and thus the bulk rock composition ("B") remains constant on the markers (rectangles). Melt to residuum ratio changes with decreasing temperature (with progressing time, t1-t3) and thus their chemical compositions as well. Through magma mixing, host rock melts can be incorporated by mixing markers. b) Melt extraction changes the bulk rock compositions on the markers. The dike is described with one new bulk rock composition, whereas the residuum has different bulk rock compositions (i, j) depending on the amount and composition of extracted melt. Through magma mixing, host rock melts and melts from a sill form a common dike, with a bulk rock composition averaged from all extracted melts.

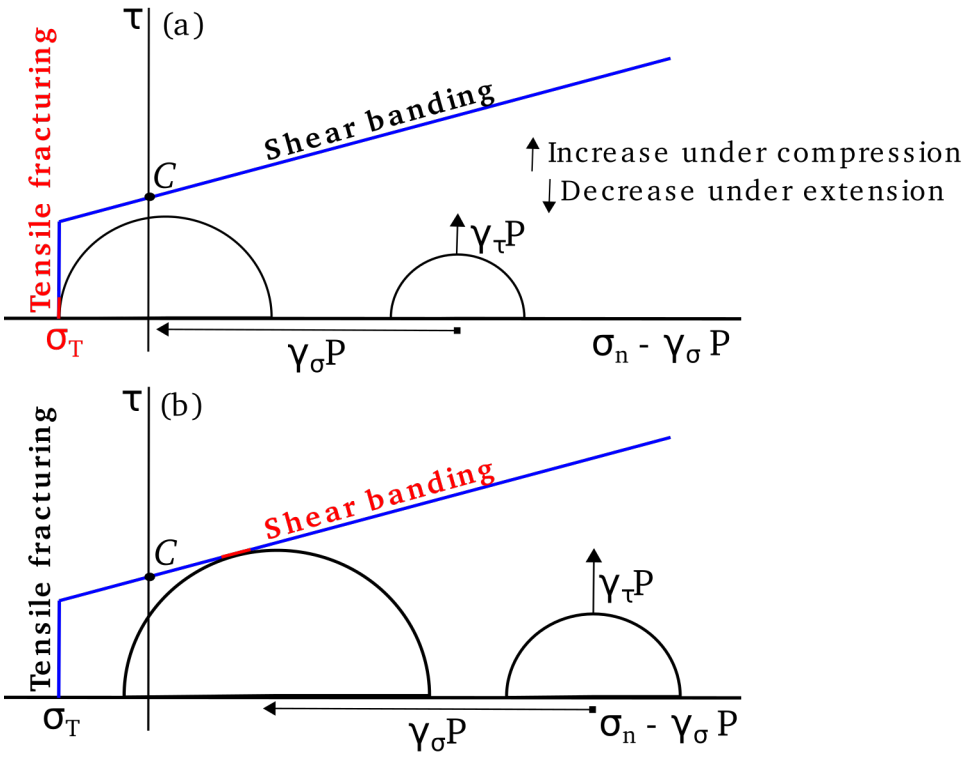

Fig. 5. Rock failure for (a) tensile fracturing and (b) shear banding. C = cohesion; σ_T = tensile strength; σ_n = normal stress, P = fluid pressure and τ = shear stress. The shift of the Mohr circle is controlled by P and γ_σ (eq. 13). The radius is controlled by the ratio of the normal stresses σ_1 and σ_3 (here as σ_h and σ_v), P and γ_τ (eq. 14) and increases under compressional and decreases under extensional conditions. The cohesion defines the intercept.

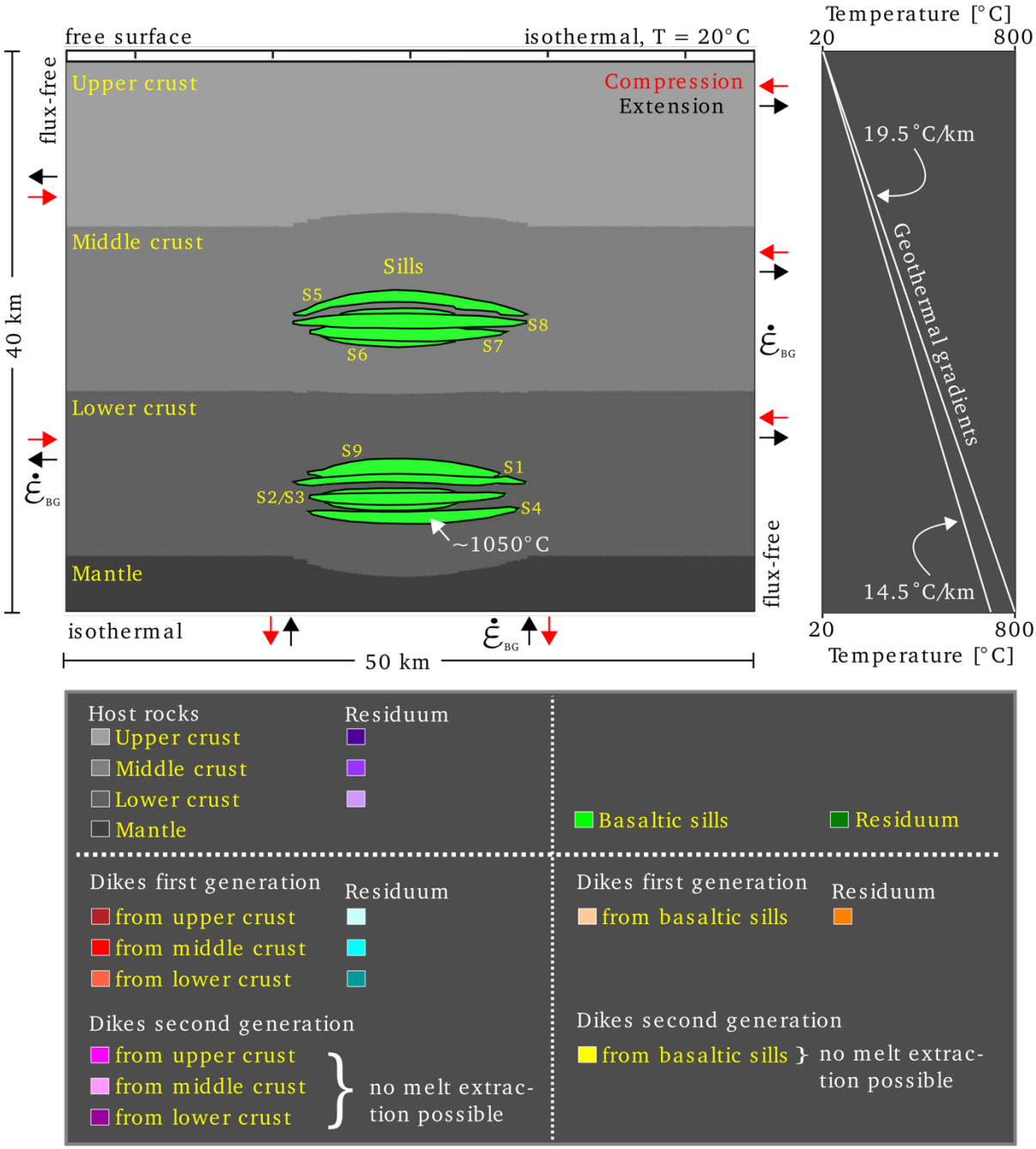

Fig. 6. Initial 2D numerical model configuration. The thermal and mechanical boundary conditions used are described in the main text. The range of depth-dependent temperature distribution is shown with the two employed geothermal gradients. Basaltic sills are periodically injected at varying depth levels (here, S1-S9) with constant temperatures of 900-1200 °C for each individual sill. After melt extraction, residual material (cumulate rocks) remains. Melt can be extracted from dikes of the first generation, but not from those of the second generation, whose melts originate from dikes of the first generation.

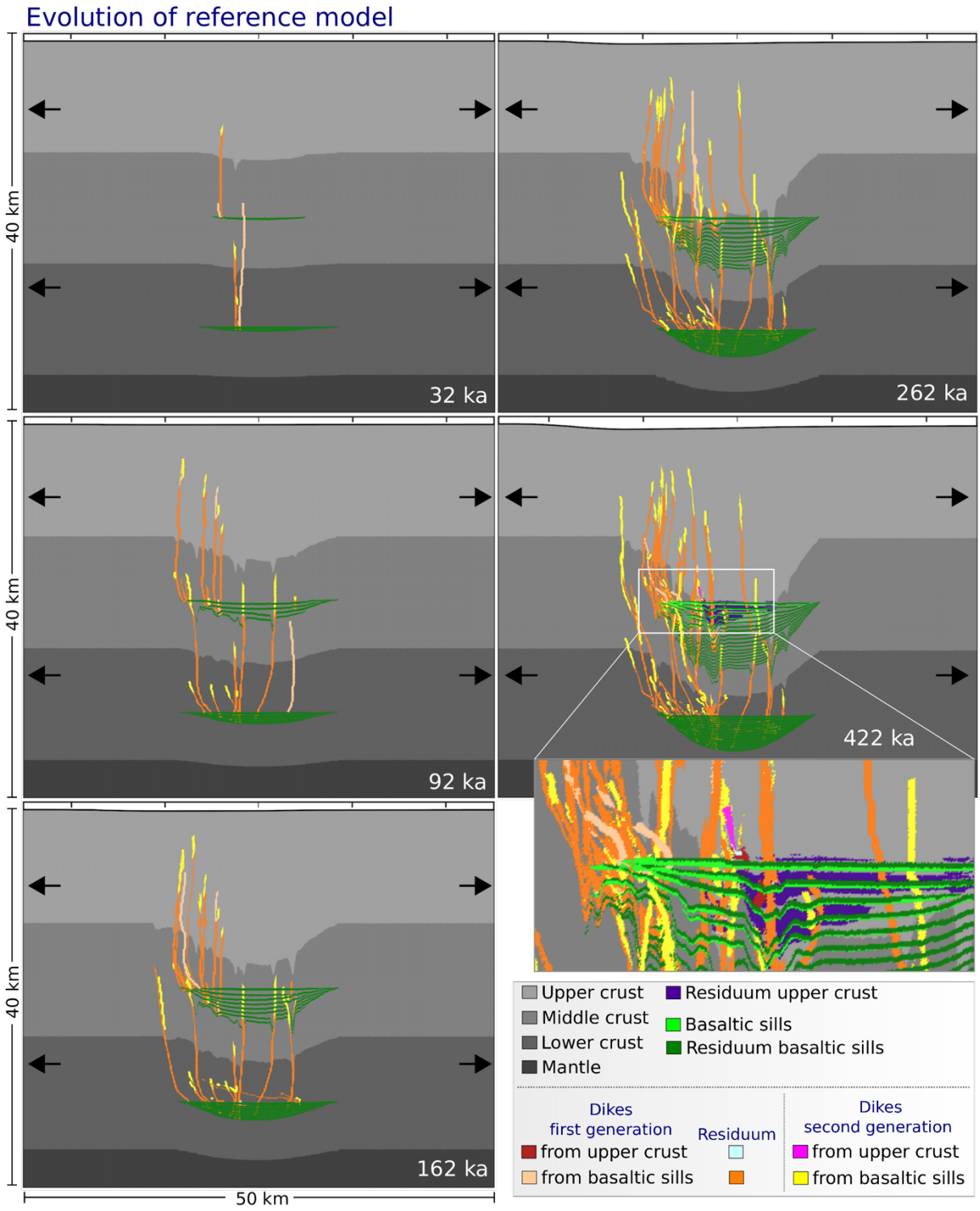

Fig. 7. Evolution of the reference simulation (model 19, Table 2). Sills are periodically injected every 10 ka (36 in total) into either the middle or the lower crust at prescribed depths. Employed extensional background strain rate = 10^{-15} s^{-1} and rock cohesion = 10 MPa. Intrusion temperature of the basaltic sills = 1050 °C and bottom temperature of the model domain (T_{bottom}) is set to 800 °C (initial geotherm at 40 km depth). The sills are injected with an initial thickness of ~0.5 km.

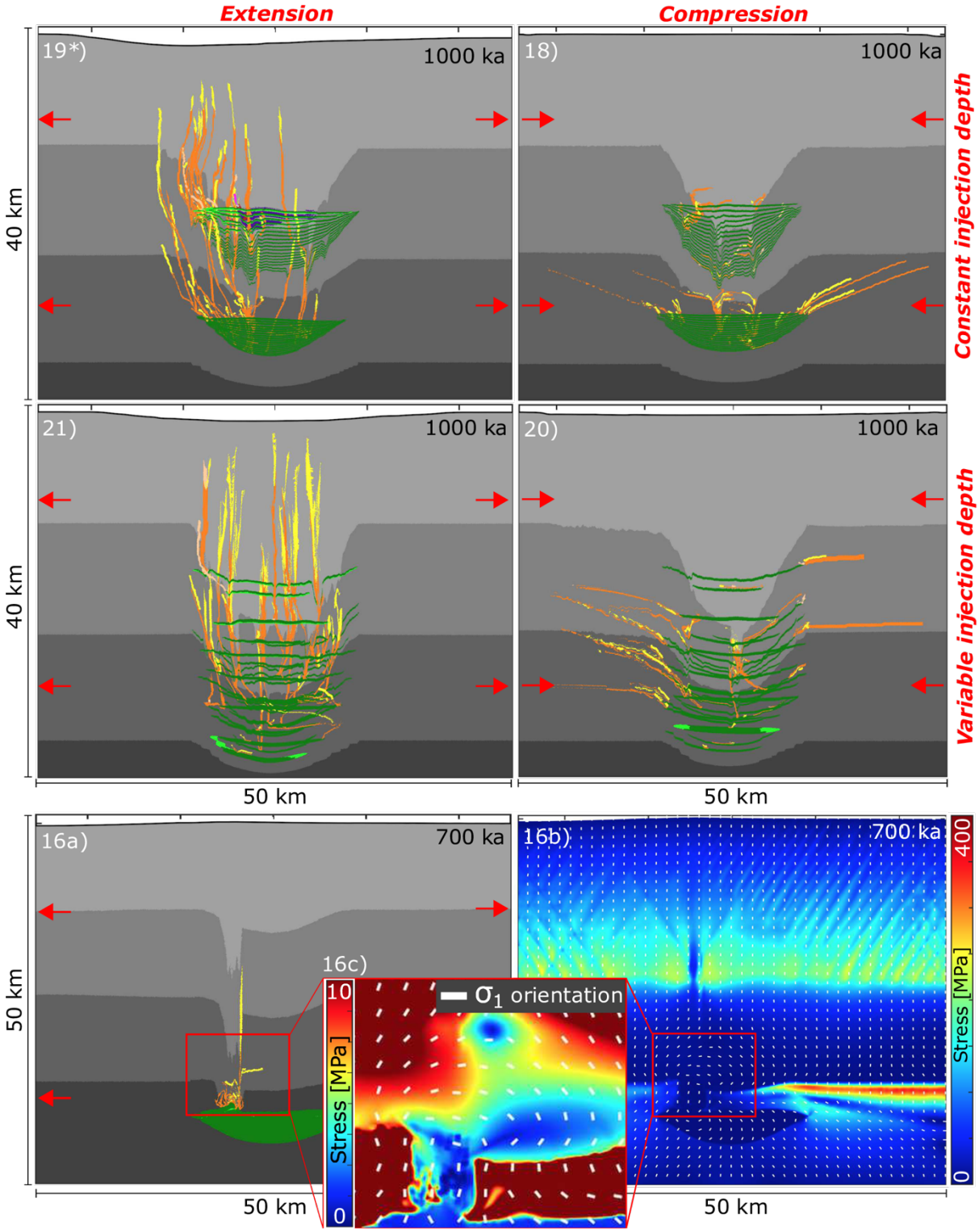

Fig. 8. Snapshots (after 1000 or 700 ka) of the magmatic systems with differently oriented dikes. The used parameters are described in Table 2. The colour legend of the rock phases is presented in Figure 6. Models 19, 21 and 16 are under extensional background strain rates and produce mainly vertically orientated dikes; Models 18 and 20 are under compressional conditions and produce mainly horizontally orientated dikes. Sill injection depths are constant for the respective zones (models 19, 18 and 16) and variable for models 21 and 20. The produced stress field (stress invariant, 16b) hampers the magma transport from the uppermost mantle into shallower crustal levels by inducing a horizontal σ_1 orientation (16c).

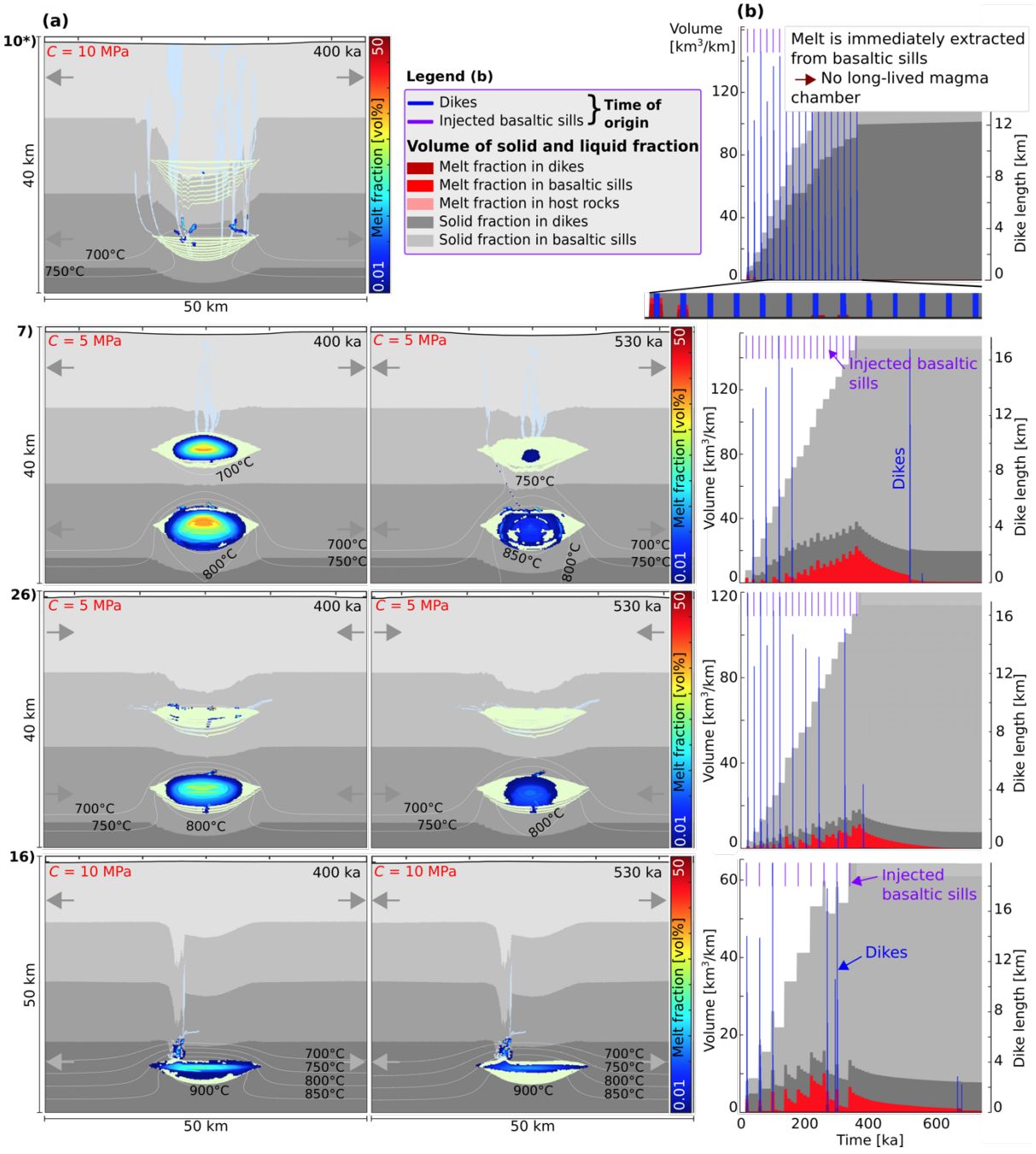

Fig. 9. Melt retention as a function of rock cohesion and injection depth. The employed parameters are described in Table 2. a) Evolution of melt fraction, shown for 400 and 530 ka. Grey arrows pointing out the background strain rate directions (extension vs. compression). b) Volume evolution of liquid and cumulate fractions with time. The blue lines show the length of the respective dikes. The purple ones indicate only the sill injection time. Model 10: Melt is extracted from basaltic sills immediately after it is injected. Models 7 and 26: Decreasing the rock cohesion (from 10 MPa to 5 MPa) stabilizes the melt fraction in the source by suppressing diking. Model 16: A deeper magma reservoir remains partially crystallized longer and keeps melt in the source.

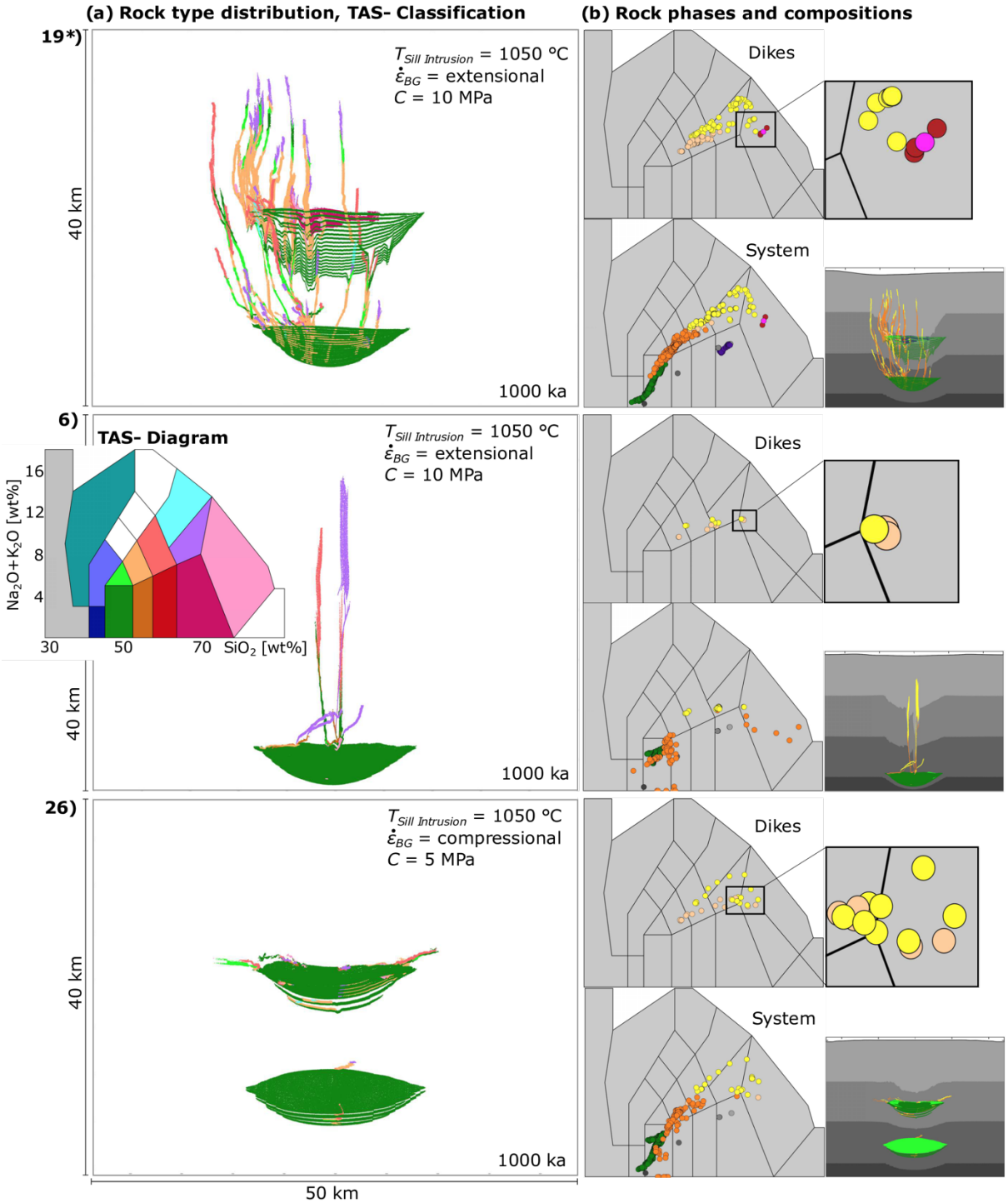

Fig. 10. Composition of the magmatic system and dikes after 1000 ka, shown with a TAS diagram classification for plutonic rocks (after Middlemost, 1994). The used parameters are described in Table 2. a) Rock types are shown with regard to the magmatic system using the TAS-classification. b) Composition of the system and dikes. The colours of the circles represent the respective rock phases (Fig. 6). With a lower rock cohesion (5 MPa, model 26) or a deeper level of intrusion (model 6), primary dikes from the sills can be highly enriched in silica through melt retention in the source (melt/cumulate ratio decreases from ~1 to ~0.05) and can be granitic in composition. In case sills directly trigger tensile fracturing, the generated primary dikes are less enriched in silica and are only quartz-monzonitic in composition (model 19).

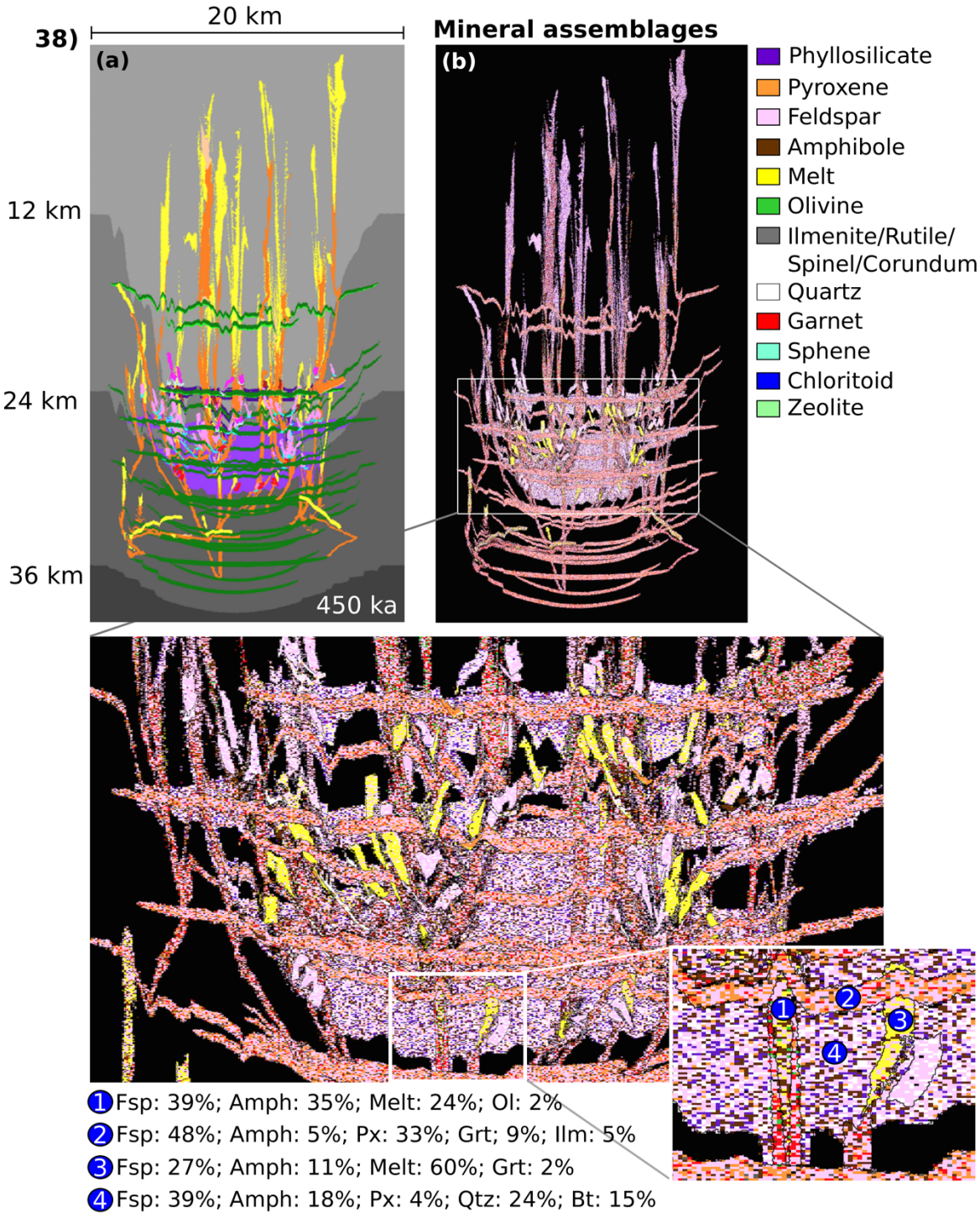

Fig. 11. Snapshot of the magmatic system after 450 ka showing the rock phases (a) and the corresponding mineral assemblages (b) of the model 38 (used parameters, Table 2). The colour legend of the rock phases is presented in Figure 6. Sills are injected under extensional conditions. The crust has a higher H_2O content (0.5, 3 and 5 wt% H_2O for the lower, middle and upper crust, Table 1). The higher H_2O content increases the amount of extracted melt from the host rocks. The phase assemblages are listed for selected domains (1-4). These domains do not necessarily correlate with the average compositions mentioned in the main text as they are only local features including the melt phase. Feldspar (Fsp), amphibole (Amph), olivine (Ol), pyroxene (Px), garnet (Grt), ilmenite (Ilm), quartz (Qtz) and biotite (Bt). Proportions are given in vol%.

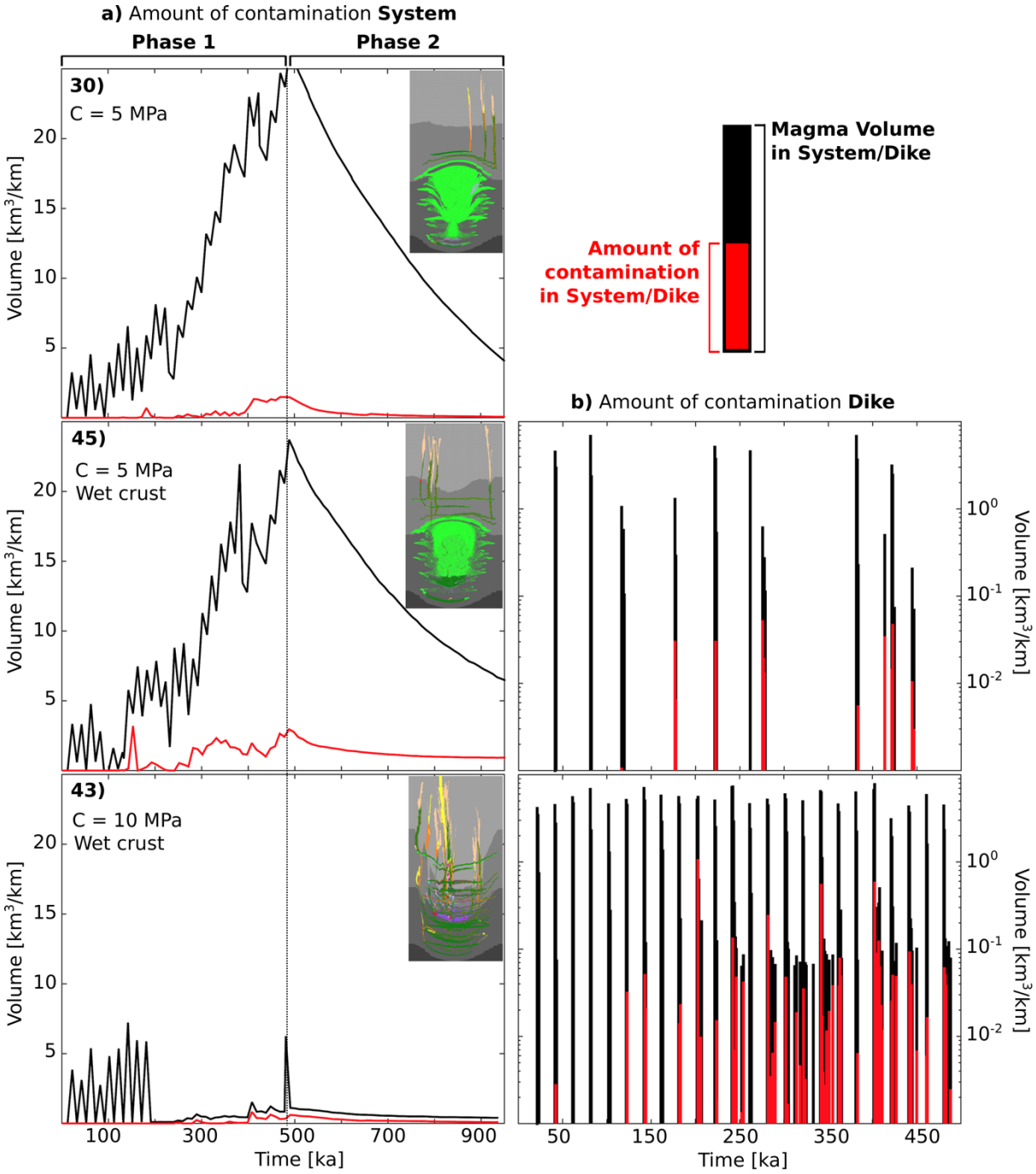

Fig. 12. Contamination of dikes and system. a) Contamination evolution of the mafic sill complex by surrounded host rocks. Phase 1 represents the stage in which sills are continuously injected (every 20 ka) to construct the mush chamber if melt is not extracted. Phase 2 represents the stage of the evolution which is characterized by the cooling of the system (no heat supply). The black line indicates the total melt volume in the system and the red line shows how much of the system is contaminated by host rocks. b) Evolution of the dikes, melt volume at their formation (black lines) and their respective amount of contamination through assimilated host rocks (red lines). The used parameters are described in Table 2.

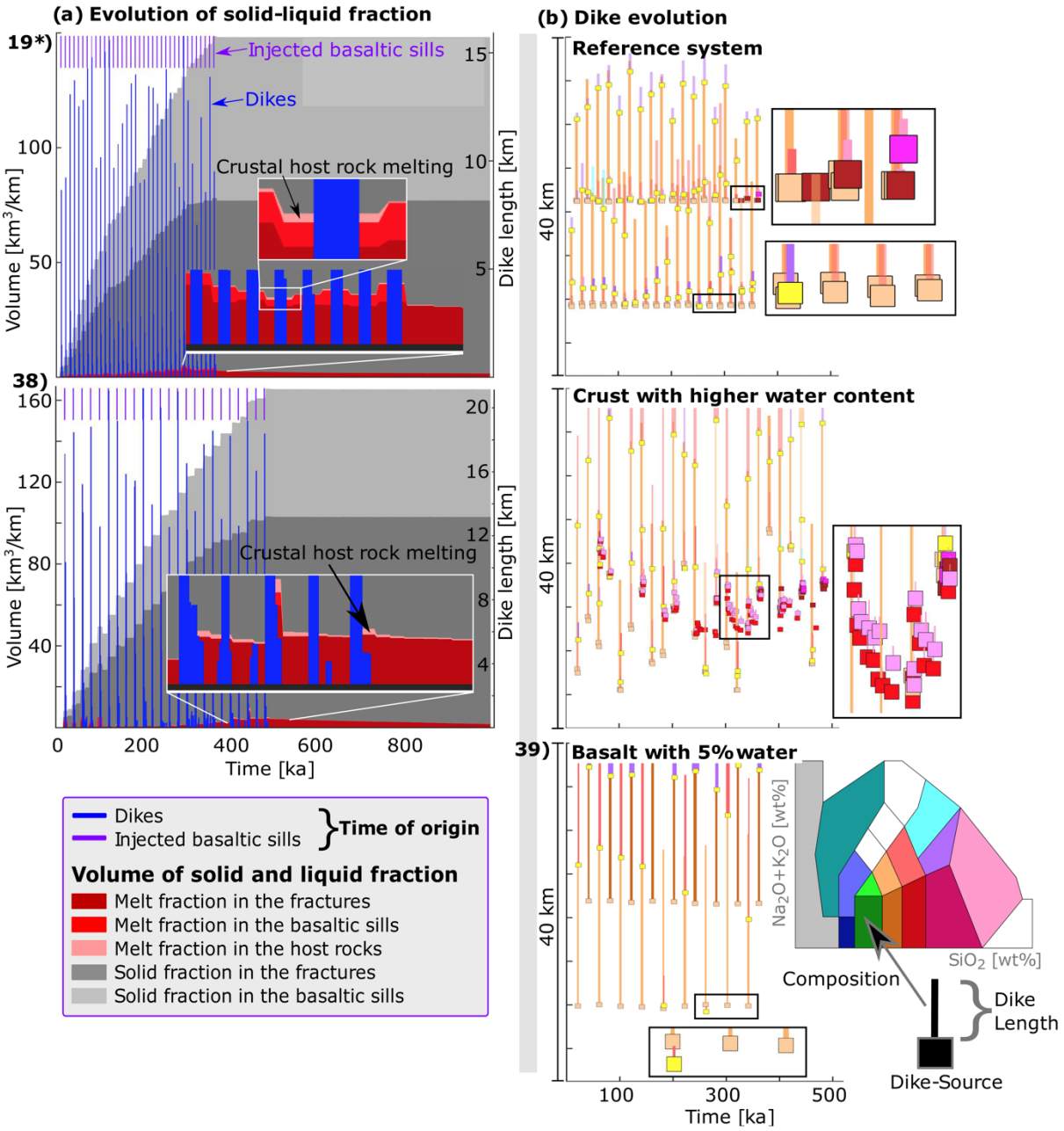

Fig. 13. Influence of H_2O content on melting and fracture formation. a) Volume evolution of liquid and cumulate fractions with time (models 19 and 38). The length of the blue lines shows the length of the respective dikes. The purple ones indicate only the sill injection time. b) Initiation times and properties of the dikes. Dike source is indicated by the coloured squares (see colour in Fig. 6) and dike compositions are presented with colours used for the TAS classification. Partial melting of host rocks is illustrated with red and pink squares. The used parameters are described in Table 2. The H_2O content of the injected basalt increases from 1 wt% for the models 19 and 38 to 5 wt% for the model 39. The crust in model 38 is enriched in H_2O (upper crust: 5 wt%; middle crust: 3 wt%; lower crust: 0.5 wt% H_2O, Table 1).

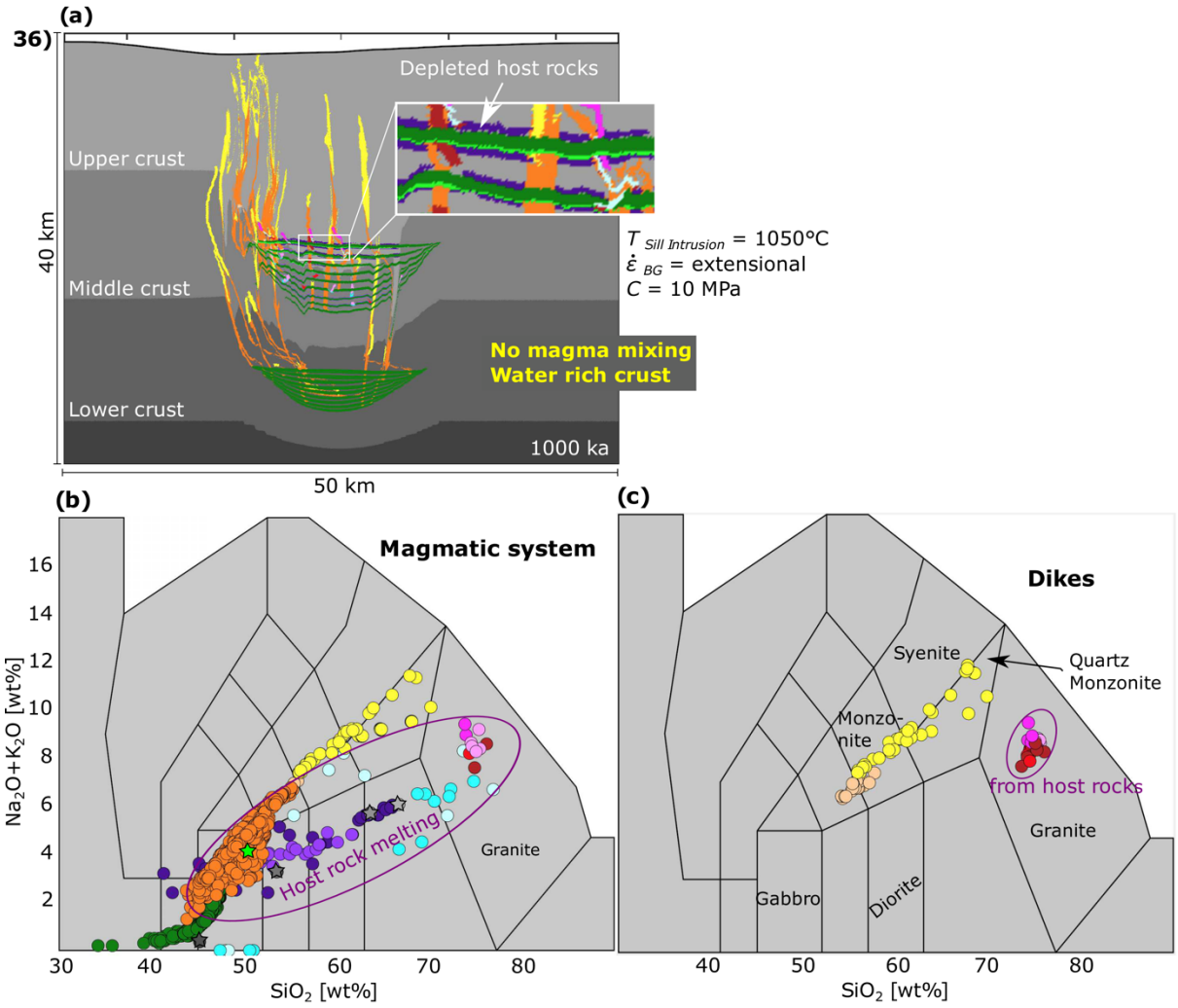

Fig. 14. Snapshot of the magmatic system after 1000 ka with a H_2O-rich upper (5 wt% H_2O), middle (3 wt% H_2O) and lower crust (0.5 wt% H_2O). Melts from the host rocks are extracted mostly from areas around the heat providing sills (a). Compositions of the system (b) and of the generated dikes (c) are shown on a TAS diagram for plutonic rocks (after Middlemost, 1994). The colours of the circles and in (a) represent the respective rock phases (Fig. 6). In blueish-purple those from host rock partial melting. Initial rock compositions are shown as stars. The parameters used for the model 36 are described in Table 2.

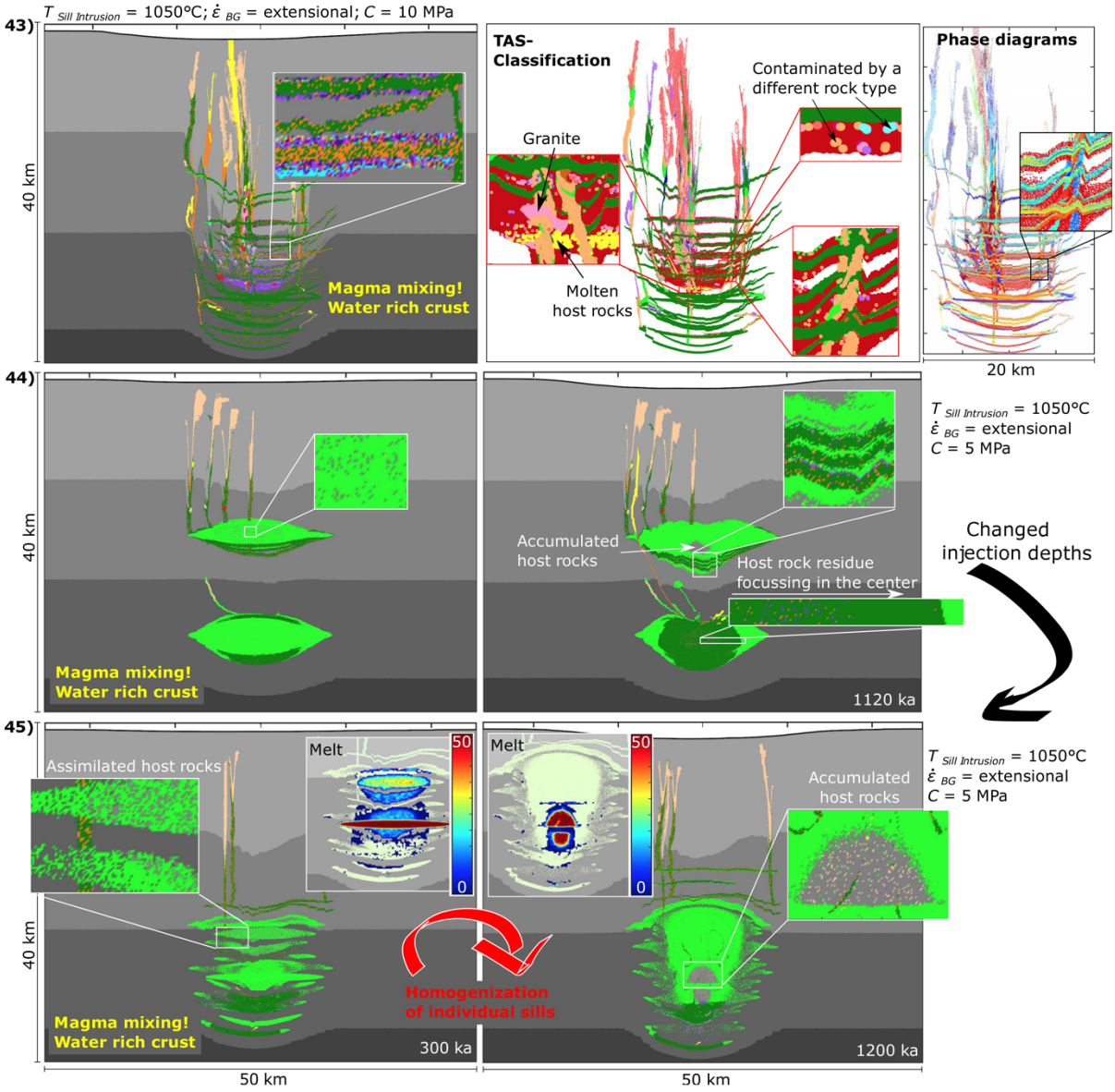

Fig. 15. Assimilation of hydrated crustal host rocks due to magma mixing or mingling processes at different times. Melt-carrying markers are randomly mixed in connected partially molten/crystallized regions. The initial crustal host rocks have a higher H_2O content (upper crust 5 wt%, middle crust 3 wt% and lower crust 0.5 wt% H_2O, Table 1). The used parameters are described in Table 2. The colour legend of the rock phases is presented in Figure 6. The rock cohesion decreases from 10 MPa (model 43) to 5 MPa (models 44 and 45). Model 43: Assimilation of host rocks is limited due to the immediate melt extraction after sill injection. The updated phase diagrams are shown (top right), with each colour representing a different employed phase diagram (4951 in total). Rock type classification (top middle) is shown with TAS diagram nomenclature (see colours in Fig. 10a). Models 44 and 45: Crustal host rocks are assimilated into the long-lived mush chamber (partially crystallized region of the injected sills).

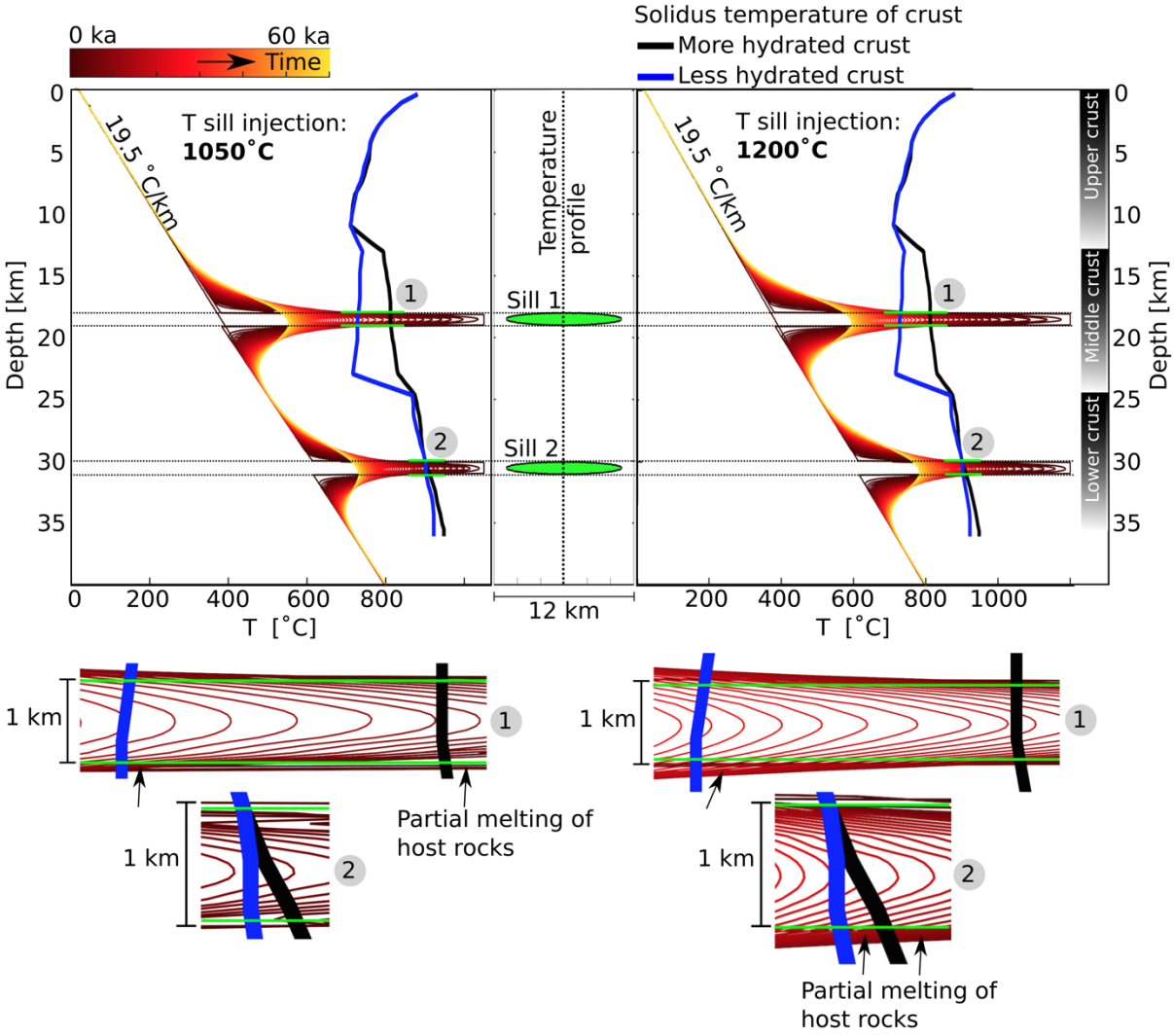

Fig. 16. Temperature evolution around sills and the effect of host rock partial melting. Two sills are emplaced in the middle and lower crust with the same intrusion temperature (1050˚C or 1200˚C). Coloured lines represent the temperature evolution with time along the middle cross profile. The initial geothermal gradient in the host rocks is 19.5 ˚C/km. The change of the solidus temperature with depth is shown for two different crust types (black line for the H_2O-rich case and blue line for the H_2O-poor case, see Table 1). Zoom-in areas (1 and 2) show in detail the partial melting zone of the host rocks (above the sill, green lines, and at temperatures higher than the respective solidus). This zone, in which the temperature is high enough to partially melt the surrounding host rocks, is limited to a few hundreds of meters.

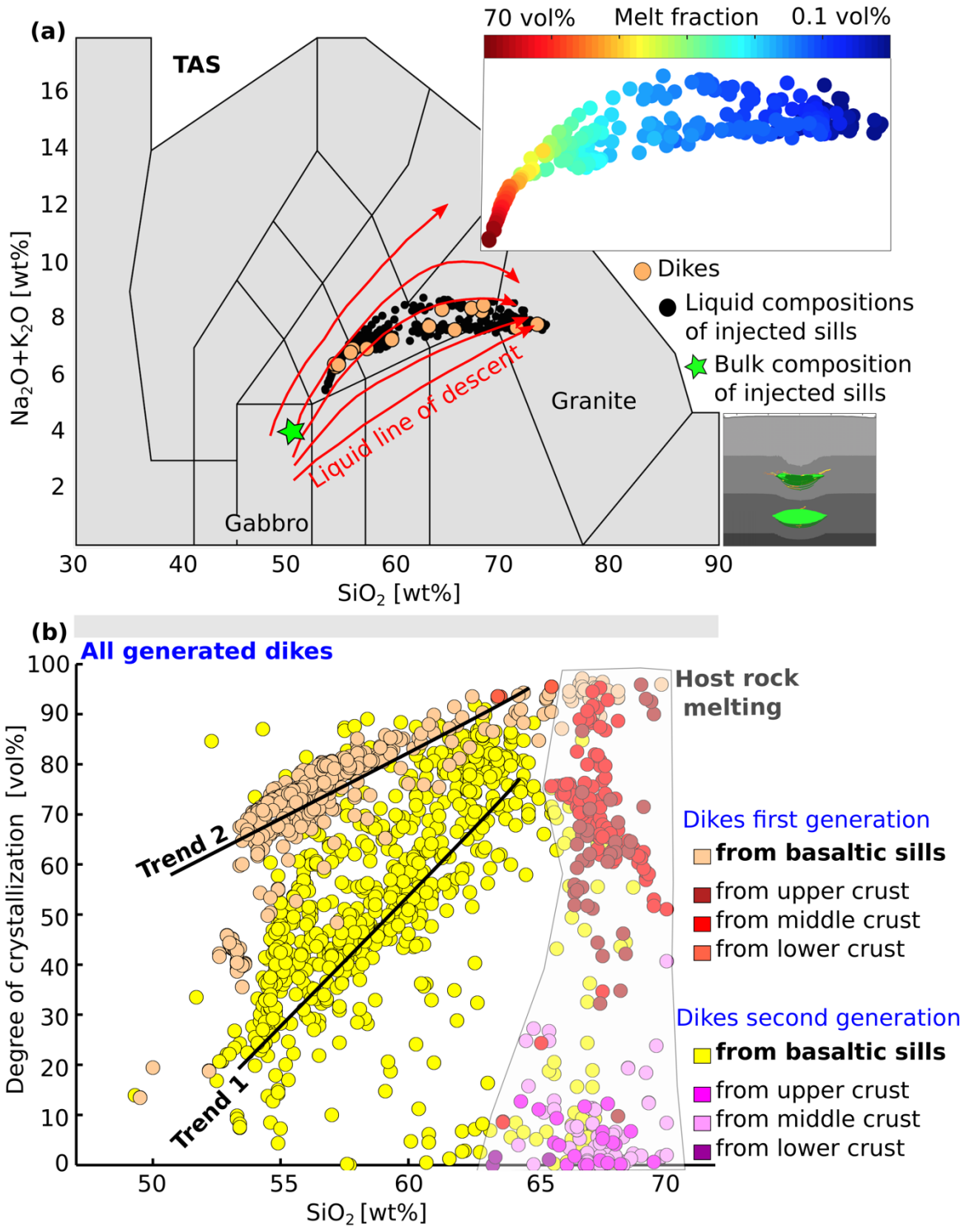

Fig. 17. a) TAS diagram for plutonic rocks (after Middlemost, 1994). Evolving liquid compositions (black-filled circles) and corresponding melt fractions from the cooling modelled magma reservoirs generated by injection and amalgamation of different sills (model 26, Fig. 9 and Fig. 10). Melt is extracted from the system to form dikes, and their compositions (orange-filled circles) are located on the respective liquid line of descent. As long as melt is not extracted, only equilibrium crystallization occurs (black-filled circles) and host rock partial melting and magma mixing is not included here. Red lines show liquid lines of descent for typical igneous rock suites (after Middlemost, 1994). b) Crystallization degree of the source

[in vol%] vs. SiO_2 concentration of dikes from all executed geodynamic simulations. The SiO_2 concentrations of the dikes are correlated with the degree of crystallization (trends are indicated by the two black lines) except for dikes generated from the crustal host rocks.

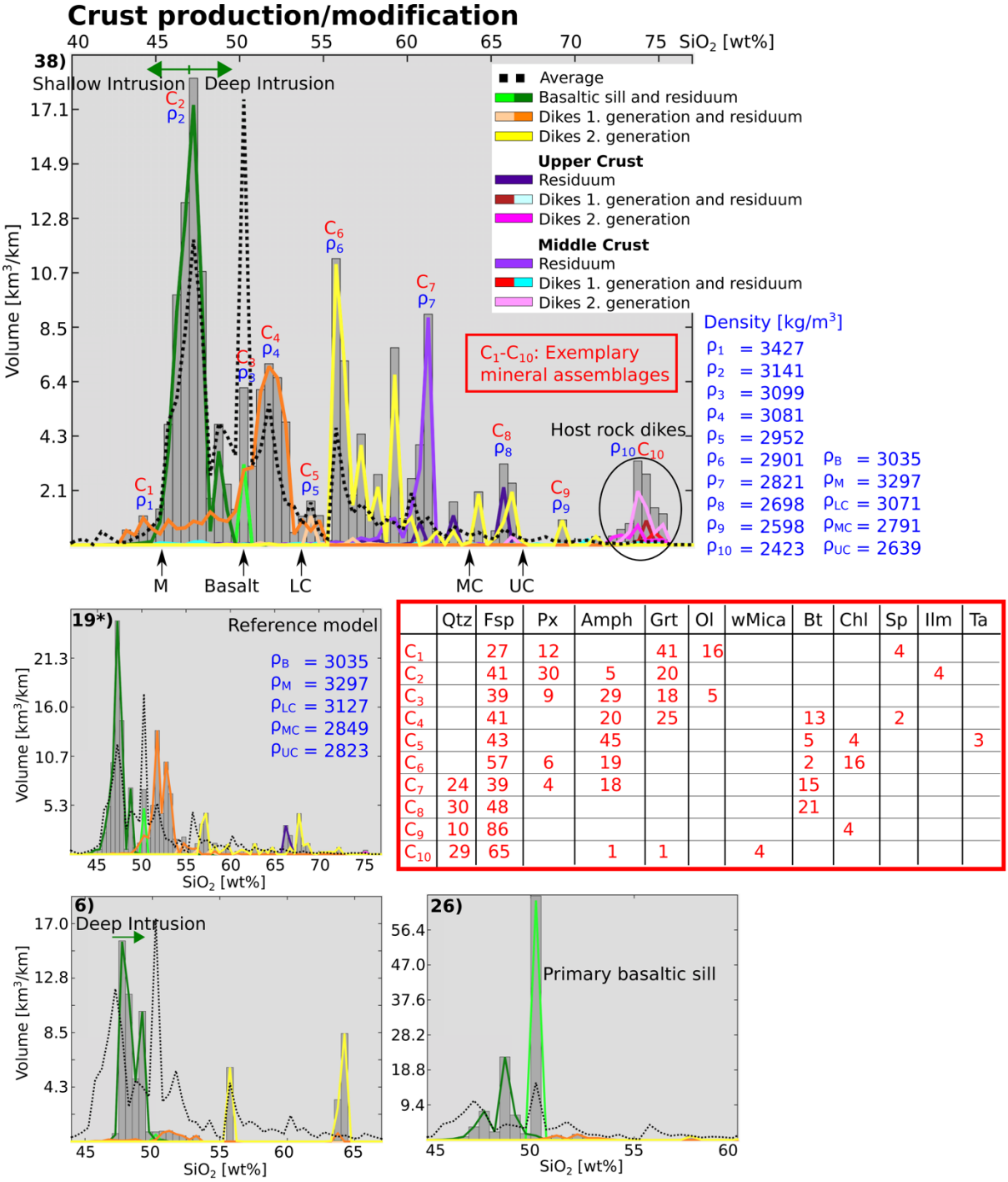

	Qtz	Fsp	Px	Amph	Grt	Ol	wMica	Bt	Chl	Sp	Ilm	Ta
C_1		27	12		41	16				4		
C_2		41	30	5	20						4	
C_3		39	9	29	18	5						
C_4		41		20	25			13		2		
C_5		43		45				5	4			3
C_6		57	6	19				2	16			
C_7	24	39	4	18				15				
C_8	30	48						21				
C_9	10	86							4			
C_{10}	29	65		1	1		4					

Fig. 18. Volume of different crust contributions from sills, cumulates, dikes, and modified crustal host rocks, and their SiO_2 concentrations (normalized without H_2O). For the histogram, 90 bins are used, each with a width of 0.5 wt% SiO_2. The total amount of newly-created or modified crust is presented as grey bars. The coloured lines represent the contributions of the respective rock phases (Fig. 6). The black dashed line is the average from all executed geodynamic simulations. The used parameters are described in Table 2. SiO_2 concentrations of

the basalt (B) and of the initial mantle (M), upper (UC), middle (MC) and lower crust (LC) are provided. Densities are given for selected bins (ρ_1-ρ_{10}) and for the initial injected (now crystallized) basalt as well as for the mantle and for the upper, middle and lower crust. Exemplary mineral assemblages are specified for the selected bins (C_1-C_{10}). Qtz (quartz), Fsp (feldspar), Px (pyroxene), Amph (amphibole), Grt (garnet), Ol (olivine), wMica (white mica), Bt (biotite), Chl (chlorite), Sp (spinel), Ilm (ilmenite), Ta (talc), given in vol%.

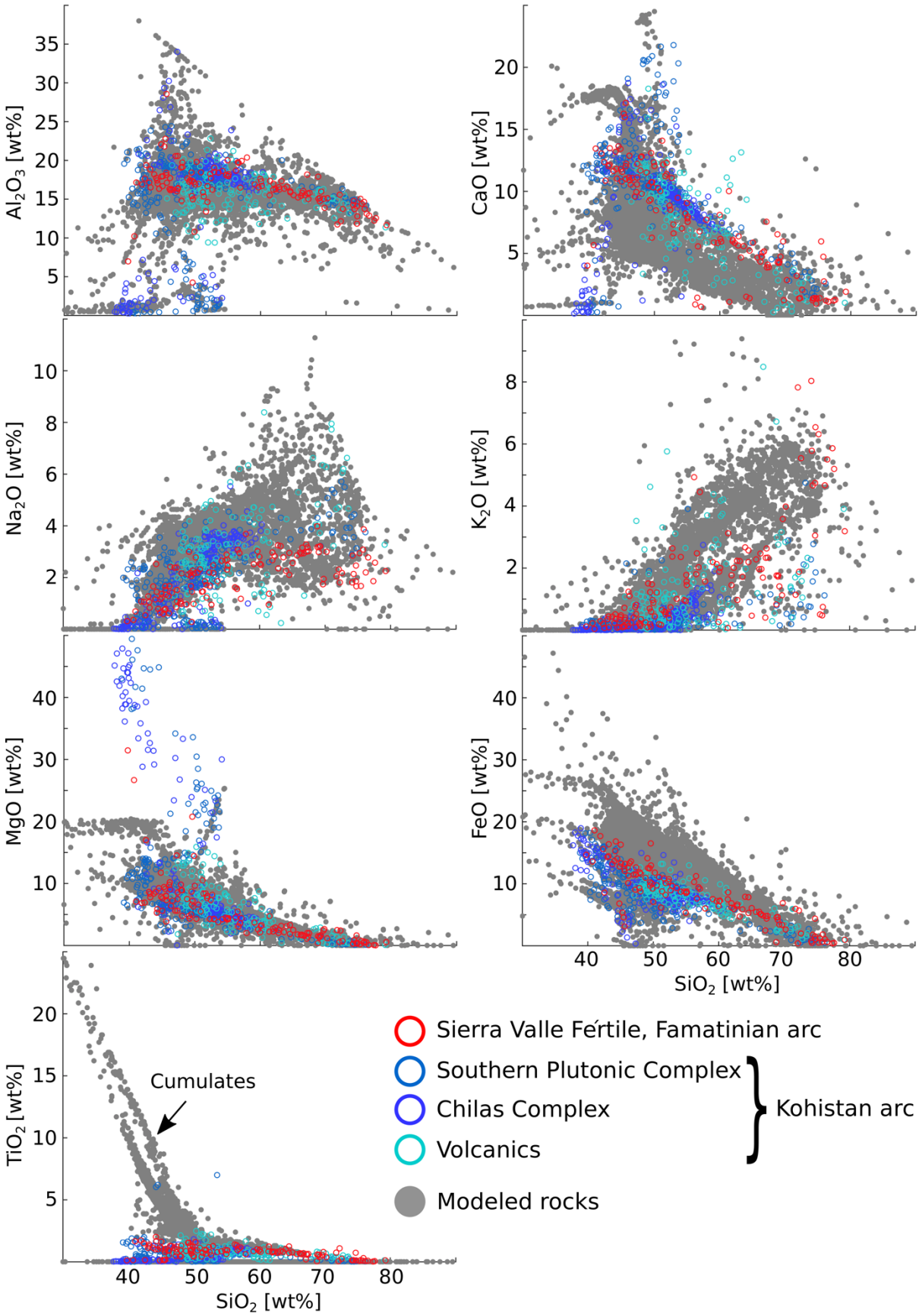

Fig 19. Comparison of igneous rocks generated in all petro-thermo-mechanical models with exposed rocks from the Famatinian and Kohistan arc. Rock compositions are on a LOI (loss

on ignition) free basis. Magmatic rock compositions of the Famatinian arc are from Otamendi et al. (2009a,b, 2010a,b, 2012) and Walker Jr et al. (2015). Rock compositions of the Kohistan arc are summarized in Jagoutz et al. (2011) and are based on the works of Jan and Howie (1981), Khan (1988), Miller and Christensen (1994), Yamamoto and Yoshino (1998), Shah and Shervais (1999), Mikoshiba et al. (1999), Rolland et al. (2002), Bignold and Treloar (2003), Garrido et al. (2006), Jagoutz et al. (2006, 2011), Takahashi et al. (2007) and Dhuime et al. (2007, 2009).

Table 1: Initial rock compositions used in Perple_X. Pyrolitic mantle (pyrolite model, McDonough and Sun, 1995), where K_2O, TiO_2, MnO, NiO and P_2O_5 are excluded. Basalt (Le Maitre, 1976), MnO, P_2O_5 and CO_2 are excluded. Upper (UC), middle (MC) and lower (LC) crust (Rudnick and Gao, 2003), MgO and P_2O_5 are excluded. H_2O is added to the crustal and basaltic compositions, respectively. Oxides are given in wt%.

Oxide	**Mantle**	**Basalt**		**LC**		**MC**		**UC**	
SiO_2	45.18	49.94	47.92	53.46	53.25	63.35	61.76	66.06	63.39
TiO_2	0.00	1.87	1.79	0.82	0.82	0.69	0.67	0.63	0.61
Al_2O_3	4.47	15.98	15.33	16.92	16.85	14.96	14.59	15.27	14.65
Cr_2O_3	0.39	0.00	0.00	0.00	0.00	0.00	0.00	0.00	0.00
FeO	8.08	10.70	10.27	8.58	8.55	6.01	5.85	5.00	4.80
MgO	37.95	6.83	6.56	7.25	7.22	3.58	3.49	2.46	2.36
CaO	3.56	9.61	9.22	9.60	9.56	5.24	5.11	3.56	3.42
Na_2O	0.36	2.95	2.83	2.65	2.64	3.38	3.30	3.24	3.11
K_2O	0.00	1.12	1.07	0.61	0.61	2.29	2.24	2.78	2.66
H_2O	0.00	1.00	5.00	0.10	0.50	0.50	3.00	1.00	5.00

Table 2: Employed parameters used in the presented models. The background strain rate ($\dot{\varepsilon}_{BG}$) is 10^{-15} s^{-1} and can either be compressional or extensional. Basaltic sills are injected with a prescribed initial temperature ($T_{Sill\ Intrusion}$) and thickness (*Sill thickness*). They are injected at chosen depths (*Injection depths*) with a frequency defined in *Injection frequency*. LC = lower crust, MC = middle crust and UM = uppermost mantle. If two injection depths are listed (e.g., LC and MC), sills are injected into both of those depth levels. Variable: Sills are distributed over middle to lower crustal depths. The total number of injections is described in *Number of injections*. T_{bottom} is the geotherm at the model bottom. *Wet crust/basalt*: Initial rock compositions with a higher water content are employed (Table 1).

Model	$T_{Sill\ Intrusion}$ [°C]	*Cohesion* [MPa]	$\dot{\varepsilon}_{BG}$	Number of injections	Injection frequency [ka]	Injection depths	Sill thickness [km]	T_{bottom} [°C]	Wet crust	Wet basalt	Magma mixing
6	1050	10	exten.	9	40	LC	~1	800	no	no	no
7	1050	5	exten.	18	20	LC and MC	~1	800	no	no	no
10*	1050	10	exten.	18	20	LC and MC	~1	800	no	no	no
12	900	10	exten.	9	40	LC	~1	800	no	no	no
16	1050	10	exten.	9	40	UM	~1	900	no	no	no
18	1050	10	compr.	36	10	LC and MC	~0.5	800	no	no	no
19*	1050	10	exten.	36	10	LC and MC	~0.5	800	no	no	no
20	1050	10	compr.	23	20	variable	~1	800	no	no	no
21	1050	10	exten.	23	20	variable	~1	800	no	no	no
26	1050	5	compr.	18	20	LC and MC	~1	800	no	no	no
28	1200	10	exten.	9	40	LC	~1	800	no	no	no
30	1050	5	exten.	23	20	variable	~1	800	no	no	yes
36	1050	10	exten.	18	20	LC and MC	~1	800	yes	no	no
38	1050	10	exten.	24	20	variable	~1	800	yes	no	no
39	1050	10	exten.	18	20	LC and MC	~1	800	no	yes	no
43	1050	10	exten.	24	20	variable	~1	800	yes	no	yes
44	1050	5	exten.	18	20	LC and MC	~1	800	yes	no	yes

REFERENCES

Annen, C., Blundy, J. D., Leuthold, J., Sparks, R. S. J., 2015. Construction and evolution of igneous bodies: Towards an integrated perspective of crustal magmatism. Lithos 230, 206-221.

Bachmann, O., Bergantz, G. W., 2004. On the origin of crystal-poor rhyolites: extracted from batholithic crystal mushes. Journal of Petrology 45 (8), 1565-1582.

Bachmann, O., Huber, C., 2016. Silicic magma reservoirs in the Earth's crust. American Mineralogist 101 (11), 2377-2404.

Bergantz, G., Schleicher, J., Burgisser, A., 2015. Open-system dynamics and mixing in magma mushes. Nature Geoscience 8 (10), 793.

Biggs, J., Pritchard, M. E., 2017. Global volcano monitoring: what does it mean when volcanoes deform? Elements 13 (1), 17-22.

Bignold, S., Treloar, P., 2003. Northward subduction of the Indian Plate beneath the Kohistan island arc, Pakistan Himalaya: new evidence from isotopic data. Journal of the Geological Society 160 (3), 377-384.

Blundy, J. D., Annen, C. J., 2016. Crustal magmatic systems from the perspective of heat transfer. Elements 12 (2), 115-120.

Burg, J.-P., Gerya, T., 2005. The role of viscous heating in Barrovian metamorphism of collisional orogens: thermomechanical models and application to the Lepontine Dome in the Central Alps. Journal of Metamorphic Geology 23 (2), 75-95.

Caricchi, L., Blundy, J., 2015. The temporal evolution of chemical and physical properties of magmatic systems. Geological Society, London, Special Publications 422, SP422-11.

Cashman, K. V., Sparks, R. S. J., Blundy, J. D., 2017. Vertically extensive and unstable magmatic systems: a unified view of igneous processes. Science 355 (6331), eaag3055.

Clemens, J., Mawer, C., 1992. Granitic magma transport by fracture propagation. Tectonophysics 204 (3-4), 339-360.

Coleman, D. S., Mills, R. D., Zimmerer, M. J., 2016. The pace of plutonism. Elements 12 (2), 97-102.

Connolly, J., 2009. The geodynamic equation of state: what and how. Geochemistry, Geophysics, Geosystems 10 (10).

Connolly, J. A., 2005. Computation of phase equilibria by linear programming: a tool for geodynamic modeling and its application to subduction zone decarbonation. Earth and Planetary Science Letters 236 (1), 524-541.

Cooper, K. M., 2017. What Does a Magma Reservoir Look Like? The "Crystal's-Eye" View. Elements 13 (1), 23-28.

De Silva, S. L., Riggs, N. R., Barth, A. P., 2015. Quickening the pulse: Fractal tempos in continental arc magmatism. Elements 11 (2), 113-118.

Dhuime, B., Bosch, D., Bodinier, J.-L., Garrido, C., Bruguier, O., Hussain, S. S., Dawood, H., 2007. Multistage evolution of the Jijal ultramafic-mafic complex (Kohistan, N Pakistan): implications for building the roots of island arcs. Earth and Planetary Science Letters 261 (1-2), 179-200.

Dhuime, B., Bosch, D., Garrido, C. J., Bodinier, J.-L., Bruguier, O., Hussain, S. S., Dawood, H., 2009. Geochemical architecture of the lower-to middle-crustal section of a paleo-island arc (Kohistan Complex, Jijal-Kamila area, northern Pakistan): implications for the evolution of an oceanic subduction zone. Journal of Petrology 50 (3), 531-569.

Duesterhoeft, E., Quinteros, J., Oberhaensli, R., Bousquet, R., de Capitani, C., 2014. Relative impact of mantle densification and eclogitization of slabs on subduction dynamics: A numerical thermodynamic/thermokinematic investigation of metamorphic density evolution. Tectonophysics 637, 20-29.

Dufek, J., Bachmann, O., 2010. Quantum magmatism: Magmatic compositional gaps generated by melt-crystal dynamics. Geology 38 (8), 687-690.

Dufek, J., Bergantz, G., 2005. Lower crustal magma genesis and preservation: a stochastic framework for the evaluation of basalt-crust interaction. Journal of Petrology 46 (11), 2167-2195.

Ellis, B. S., Bachmann, O., Wolff, J. A., 2014. Cumulate fragments in silicic ignimbrites: The case of the Snake River Plain. Geology 42 (5), 431-434.

Garrido, C. J., Bodinier, J.-L., Burg, J.-P., Zeilinger, G., Hussain, S. S., Dawood, H., Chaudhry, M. N., Gervilla, F., 2006. Petrogenesis of mafic garnet granulite in the lower crust of the Kohistan paleo-arc complex (Northern Pakistan): implications for intra-crustal differentiation of island arcs and generation of continental crust. Journal of Petrology 47 (10), 1873-1914.

Gerbault, M., Hassani, R., Novoa Lizama, C., Souche, A., 2018. Three-Dimensional Failure Patterns Around an Inflating Magmatic Chamber. Geochemistry, Geophysics, Geosystems 19 (3), 749-771.

Gerya, T. V., Yuen, D. A., 2007. Robust characteristics method for modelling multiphase visco-elasto-plastic thermo-mechanical problems. Physics of the Earth and Planetary Interiors 163 (1), 83-105.

Green, E., White, R., Diener, J., Powell, R., Holland, T., Palin, R., 2016. Activity-composition relations for the calculation of partial melting equilibria in metabasic rocks. Journal of Metamorphic Geology 34 (9), 845-869.

Gudmundsson, A., 2006. How local stresses control magma-chamber ruptures, dyke injections, and eruptions in composite volcanoes. Earth-Science Reviews 79 (1-2), 1-31.

Hebert, L. B., Antoshechkina, P., Asimow, P., Gurnis, M., 2009. Emergence of a low-viscosity channel in subduction zones through the coupling of mantle flow and thermodynamics. Earth and Planetary Science Letters 278 (3-4), 243-256.

Hildreth, W., Moorbath, S., 1988. Crustal contributions to arc magmatism in the Andes of central Chile. Contributions to mineralogy and petrology 98 (4), 455-489.

Hill, G. J., Caldwell, T. G., Heise, W., Chertkoff, D. G., Bibby, H. M., Burgess, M. K., Cull, J. P., Cas, R. A., 2009. Distribution of melt beneath Mount St Helens and Mount Adams inferred from magnetotelluric data. Nature Geoscience 2 (11), 785.

Hirth, G., Kohlstedt, D., 2003. Rheology of the upper mantle and the mantle wedge: A view from the experimentalists. Inside the subduction Factory, 83–105.

Holland, T. J. B., Powell, R., 2011. An improved and extended internally consistent thermodynamic dataset for phases of petrological interest, involving a new equation of state for solids. Journal of Metamorphic Geology, 29(3), 333-383.

Holland, T. J., Green, E. C., Powell, R., 2018. Melting of peridotites through to granites: a simple thermodynamic model in the system KNCFMASHTOCr. Journal of Petrology.

Huang, H.-H., Lin, F.-C., Schmandt, B., Farrell, J., Smith, R. B., Tsai, V. C., 2015. The Yellowstone magmatic system from the mantle plume to the upper crust. Science 348 (6236), 773-776.

Huber, C., Parmigiani, A., 2018. A Physical Model for Three-Phase Compaction in Silicic Magma Reservoirs. Journal of Geophysical Research: Solid Earth 123 (4), 2685-2705.

Jackson, M. D., Blundy, J., Sparks, R. S. J., 2018. Chemical differentiation, cold storage and remobilization of magma in the Earth's crust. *Nature*, *564*(7736), 405.

Jagoutz, O., 2014. Arc crustal differentiation mechanisms. Earth and Planetary Science Letters 396, 267-277.

Jagoutz, O., Kelemen, P. B., 2015. Role of arc processes in the formation of continental crust. Annual Review of Earth and Planetary Sciences 43, 363-404.

Jagoutz, O., Klein, B., 2018. On the importance of crystallization-differentiation for the generation of SiO2-rich melts and the compositional build-up of arc (and continental) crust. American Journal of Science 318 (1), 29-63.

Jagoutz, O., Müntener, O., Burg, J.-P., Ulmer, P., Jagoutz, E., 2006. Lower continental crust formation through focused flow in km-scale melt conduits: The zoned ultramafic bodies of the Chilas Complex in the Kohistan island arc (NW Pakistan). Earth and Planetary Science Letters 242 (3-4), 320-342.

Jagoutz, O., Müntener, O., Schmidt, M. W., Burg, J.-P., 2011. The roles of flux-and decompression melting and their respective fractionation lines for continental crust formation: Evidence from the Kohistan arc. Earth and Planetary Science Letters 303 (1-2), 25-36.

Jan, M. Q., Howie, R., 1981. The mineralogy and geochemistry of the metamorphosed basic and ultrabasic rocks of the Jijal complex, Kohistan, NW Pakistan. Journal of Petrology 22 (1), 85-126.

Jennings, E. S., Holland, T. J., 2015. A simple thermodynamic model for melting of peridotite in the system NCFMASOCr. Journal of Petrology 56 (5), 869-892.

Johnson, T. E., Brown, M., Kaus, B. J., VanTongeren, J. A., 2014. Delamination and recycling of Archaean crust caused by gravitational instabilities. Nature Geoscience 7 (1), 47-52.

Karakas, O., Dufek, J., Mangan, M. T., Wright, H. M., Bachmann, O., 2017. Thermal and petrologic constraints on lower crustal melt accumulation under the Salton Sea Geothermal Field. Earth and Planetary Science Letters 467, 10-17.

Karlstrom, L., Paterson, S. R., Jellinek, A. M., 2017. A reverse energy cascade for crustal magma transport. Nature Geoscience 10 (8), 604.

Katz, R. F., Spiegelman, M., Langmuir, C. H., 2003. A new parameterization of hydrous mantle melting. Geochemistry, Geophysics, Geosystems 4 (9).

Kaus, B. J., 2010. Factors that control the angle of shear bands in geodynamic numerical models of brittle deformation. Tectonophysics 484 (1), 36-47.

Khan, M., 1988. Petrology and structure of the Chilas ultramafic-mafic complex, Kohistan Arc, NW Himalayas. Unpublished PhD Thesis, University of London.

Kiser, E., Palomeras, I., Levander, A., Zelt, C., Harder, S., Schmandt, B., Hansen, S., Creager, K., Ulberg, C., 2016. Magma reservoirs from the upper crust to the Moho inferred from high-resolution Vp and Vs models beneath Mount St. Helens, Washington State, USA. Geology 44 (6), 411-414.

Le Maitre, R., 1976. The chemical variability of some common igneous rocks. Journal of petrology 17 (4), 589-598.

Lees, J. M., 2007. Seismic tomography of magmatic systems. Journal of Volcanology and Geothermal Research 167 (1-4), 37-56.

Leuthold, J., Müntener, O., Baumgartner, L. P., Putlitz, B., Ovtcharova, M., Schaltegger, U., 2012. Time resolved construction of a bimodal laccolith (Torres del Paine, Patagonia). Earth and Planetary Science Letters 325, 85-92.

Magni, V., Bouilhol, P., van Hunen, J., 2014. Deep water recycling through time. Geochemistry, Geophysics, Geosystems 15 (11), 4203-4216.

McDonough, W. F., Sun, S.-S., 1995. The composition of the Earth. Chemical geology 120 (3), 223-253.

McKenzie, D., 1984. The generation and compaction of partially molten rock. Journal of petrology 25 (3), 713-765.

Middlemost, E. A., 1994. Naming materials in the magma/igneous rock system. Earth-Science Reviews 37 (3-4), 215-224.

Mikoshiba, M., Takahashi, Y., Takahashi, Y., Kausar, A. B., Khan, T., Kubo, K., Shirahase, T., 1999. Rb-Sr isotopic study of the Chilas igneous complex, Kohistan, northern Pakistan. SPECIAL PAPERS-GEOLOGICAL SOCIETY OF AMERICA, 47-58.

Miller, D. J., Christensen, N. L., 1994. Seismic signature and geochemistry of an island arc: A multidisciplinary study of the Kohistan accreted terrane, northern Pakistan. Journal of Geophysical Research: Solid Earth 99 (B6), 11623-11642.

Müntener, O., Ulmer, P., 2018. Arc crust formation and differentiation constrained by experimental petrology. American Journal of Science 318 (1), 64-89.

Novoa, C., Remy, D., Gerbault, M., Baez, J. C., Tassara, A., Cordova, L., Cardona, C., Granger, M., Bonvalot, S., Delgado, F., 2019. Viscoelastic relaxation: A mechanism to explain the decennial large surface displacements at the Laguna del Maule silicic volcanic complex. Earth and Planetary Science Letters, 521, 46-59.

Oliveira, B., Afonso, J. C., Zlotnik, S., Diez, P., 2017. Numerical modelling of multiphase multicomponent reactive transport in the Earth's interior. Geophysical Journal International 212 (1), 345-388.

Otamendi, J., Cristofolini, E., Tibaldi, A., Quevedo, F., Baliani, I., 2010a. Petrology of mafic and ultramafic layered rocks from the Jaboncillo Valley, Sierra de Valle Fértil, Argentina: implications for the evolution of magmas in the lower crust of the Famatinian arc. Journal of South American Earth Sciences 29 (3), 685-704.

Otamendi, J., Pinotti, L., Basei, M. A. S., Tibaldi, A., 2010b. Evaluation of petrogenetic models for intermediate and silicic plutonic rocks from the Sierra de Valle Fértil-La Huerta, Argentina: Petrologic constraints on the origin of igneous rocks in the Ordovician Famatinian-Puna paleoarc. Journal of South American Earth Sciences 30 (1), 29-45.

Otamendi, J. E., Ducea, M. N., Bergantz, G. W., 2012. Geological, petrological and geochemical evidence for progressive construction of an arc crustal section, Sierra de Valle Fértil, Famatinian Arc, Argentina. Journal of Petrology 53 (4), 761-800.

Otamendi, J. E., Ducea, M. N., Tibaldi, A. M., Bergantz, G. W., de la Rosa, J. D., Vujovich, G. I., 2009a. Generation of tonalitic and dioritic magmas by coupled partial melting of gabbroic and metasedimentary rocks within the deep crust of the Famatinian magmatic arc, Argentina. Journal of Petrology 50 (5), 841-873.

Otamendi, J. E., Vujovich, G. I., de la Rosa, J. D., Tibaldi, A. M., Castro, A., Martino, R. D., Pinotti, L. P., 2009b. Geology and petrology of a deep crustal zone from the Famatinian paleo-arc, Sierras de Valle Fértil and La Huerta, San Juan, Argentina. Journal of South American Earth Sciences 27 (4), 258-279.

Paterson, S. R., Ducea, M. N., 2015. Arc magmatic tempos: gathering the evidence. Elements 11 (2), 91-98.

Paterson, S. R., Okaya, D., Memeti, V., Economos, R., Miller, R. B., 2011. Magma addition and flux calculations of incrementally constructed magma chambers in continental margin arcs: Combined field, geochronologic, and thermal modeling studies. Geosphere 7 (6), 1439-1468.

Paterson, S. R., Žák, J., Janoušek, V., 2008. Growth of complex sheeted zones during recycling of older magmatic units into younger: Sawmill Canyon area, Tuolumne batholith, Sierra Nevada, California. Journal of Volcanology and Geothermal Research 177 (2), 457-484.

Petford, N., Kerr, R. C., Lister, J. R., 1993. Dike transport of granitoid magmas. Geology 21 (9), 845-848.

Piccolo, A., Palin, R. M., Kaus, B. J., White, R. W. Generation of Earth's early continents from a relatively cool Archean mantle. Geochemistry, Geophysics, Geosystems.

Pichavant, M., Mysen, B., Macdonald, R., 2002. Source and H2O content of high-MgO magmas in island arc settings: an experimental study of a primitive calc-alkaline basalt from St. Vincent, Lesser Antilles arc. Geochimica et Cosmochimica Acta 66 (12), 2193-2209.

Plank, T., Kelley, K. A., Zimmer, M. M., Hauri, E. H., Wallace, P. J., 2013. Why do mafic arc magmas contain 4 wt% water on average? Earth and Planetary Science Letters 364, 168-179.

Pritchard, M. E., Gregg, P. M., 2016. Geophysical evidence for silicic crustal melt in the continents: where, what kind, and how much? Elements 12 (2), 121-127.

Putirka, K. D., 2017. Down the crater: where magmas are stored and why they erupt. Elements 13 (1), 11-16.

Riel, N., Bouilhol, P., van Hunen, J., Cornet, J., Magni, V., Grigorova, V., Velic, M., 2018. Interaction between mantle-derived magma and lower arc crust: quantitative reactive melt flow modelling using STyx. Geological Society, London, Special Publications 478, SP478-6.

Rivalta, E., Taisne, B., Bunger, A., Katz, R., 2015. A review of mechanical models of dike propagation: Schools of thought, results and future directions. Tectonophysics 638, 1-42.

Rolland, Y., Picard, C., Pecher, A., Lapierre, H., Bosch, D., Keller, F., 2002. The cretaceous Ladakh arc of NW himalaya-slab melting and melt-mantle interaction during fast northward drift of Indian Plate. Chemical Geology 182 (2-4), 139-178.

Rozhko, A., Podladchikov, Y., Renard, F., 2007. Failure patterns caused by localized rise in pore-fluid overpressure and effective strength of rocks. Geophysical Research Letters 34 (22).

Rubin, A. M., 1993. Dikes vs. diapirs in viscoelastic rock. Earth and Planetary Science Letters 119 (4), 641-659.

Rudnick, R., Gao, S., 2003. Composition of the continental crust. Treatise on geochemistry 3, 659.

Rummel, L., Kaus, B. J., White, R. W., Mertz, D. F., Yang, J., Baumann, T. S., 2018. Coupled petrological-geodynamical modeling of a compositionally heterogeneous mantle plume. Tectonophysics 723, 242-260.

Rüpke, L. H., Morgan, J. P., Hort, M., Connolly, J. A., 2004. Serpentine and the subduction zone water cycle. Earth and Planetary Science Letters 223 (1-2), 17-34.

Ruprecht, P., Plank, T., 2013. Feeding andesitic eruptions with a high-speed connection from the mantle. Nature 500 (7460), 68.

Scaillet, B., Holtz, F., Pichavant, M., 2016. Experimental constraints on the formation of silicic magmas. Elements 12 (2), 109-114.

Schmeling, H., Arndt, N., 2017. Modelling komatiitic melt accumulation and segregation in the transition zone. Earth and Planetary Science Letters 472, 95-106.

Schmeling, H., Marquart, G., Weinberg, R., Wallner, H., 2019. Modelling melting and melt segregation by two-phase flow: new insights into the dynamics of magmatic systems in the continental crust. Geophysical Journal International 217 (1), 422-450.

Shah, M. T., Shervais, J. W., 1999. The Dir-Utror metavolcanic sequence, Kohistan arc terrane, northern Pakistan. Journal of Asian Earth Sciences 17 (4), 459-475.

Sisson, T., Ratajeski, K., Hankins, W., Glazner, A., 2005. Voluminous granitic magmas from common basaltic sources. Contributions to Mineralogy and Petrology 148 (6), 635-661.

Solano, J., Jackson, M., Sparks, R., Blundy, J., 2014. Evolution of major and trace element composition during melt migration through crystalline mush: implications for chemical differentiation in the crust. American Journal of Science 314 (5), 895-939.

Solano, J., Jackson, M., Sparks, R., Blundy, J., Annen, C., 2012. Melt segregation in deep crustal hot zones: a mechanism for chemical differentiation, crustal assimilation and the formation of evolved magmas. Journal of Petrology 53 (10), 1999-2026.

Sparks, R. S. J., Cashman, K. V., 2017. Dynamic magma systems: Implications for forecasting volcanic activity. Elements 13 (1), 35-40.

Sun, R. J., 1969. Theoretical size of hydraulically induced horizontal fractures and corresponding surface uplift in an idealized medium. Journal of Geophysical Research 74 (25), 5995-6011.

Takahashi, Y., Mikoshiba, M. U., Takahashi, Y., Kausar, A. B., Khan, T., Kubo, K., 2007. Geochemical modelling of the Chilas Complex in the Kohistan Terrane, northern Pakistan. Journal of Asian Earth Sciences 29 (2-3), 336-349.

Tegner, C., Thy, P., Holness, M. B., Jakobsen, J. K., Lesher, C. E., 2009. Differentiation and compaction in the Skaergaard intrusion. Journal of Petrology 50 (5), 813-840.

Thielmann, M., Kaus, B. J., 2012. Shear heating induced lithospheric-scale localization: Does it result in subduction? Earth and Planetary Science Letters 359, 1-13.

Tirone, M., Ganguly, J., Morgan, J., 2009. Modeling petrological geodynamics in the Earth's mantle. Geochemistry, Geophysics, Geosystems 10 (4).

Ulmer, P., Kaegi, R., Müntener, O., 2018. Experimentally Derived Intermediate to Silica-rich Arc Magmas by Fractional and Equilibrium Crystallization at 1·0 GPa: an Evaluation of Phase Relationships, Compositions, Liquid Lines of Descent and Oxygen Fugacity. Journal of Petrology 59 (1), 11-58.

Vogt, K., Gerya, T. V., Castro, A., 2012. Crustal growth at active continental margins: numerical modeling. Physics of the Earth and Planetary Interiors 192, 1-20.

Walker Jr, B. A., Bergantz, G. W., Otamendi, J. E., Ducea, M. N., Cristofolini, E. A., 2015. A MASH zone revealed: the mafic complex of the Sierra Valle Fértil. Journal of Petrology 56 (9), 1863-1896.

White, R., Powell, R., Holland, T., 2001. Calculation of partial melting equilibria in the system Na2O-CaO-K2O-FeO-MgO-Al2O3-SiO2-H2O (NCKFMASH). Journal of Metamorphic Geology 19 (2), 139-153.

White, R., Powell, R., Holland, T., Johnson, T., Green, E., 2014. New mineral activity-composition relations for thermodynamic calculations in metapelitic systems. Journal of Metamorphic Geology 32 (3), 261-286.

Yamamoto, H., Yoshino, T., 1998. Superposition of replacements in the mafic granulites of the Jijal complex of the Kohistan arc, northern Pakistan: dehydration and rehydration within deep arc crust. Lithos 43 (4), 219-234.

Yamato, P., Agard, P., Burov, E., Le Pourhiet, L., Jolivet, L., Tiberi, C., 2007. Burial and exhumation in a subduction wedge: Mutual constraints from thermomechanical modeling and natural P-T-t data (Schistes Lustrés, western Alps). Journal of Geophysical Research: Solid Earth 112 (B7).